A Novel Defocused Image Segmentation Method Based on PCNN and LBP

SADIA BASAR [1,2], **MUSHTAQ ALI** [1], **GILBERTO OCHOA-RUIZ** [3], **ABDUL WAHEED** [1,4], **GERARDO RODRIGUEZ-HERNANDEZ** [5], **AND MAHDI ZAREEI** [3], (Senior Member, IEEE)

[1] Department of Information Technology, Hazara University Mansehra, Mansehra 21120, Pakistan
[2] Department of Computer Science, Abbottabad University of Science and Technology, Abbottabad 22010, Pakistan
[3] School of Engineering and Sciences, Tecnologico de Monterrey, Zapopan 45201, Mexico
[4] School of Electrical and Computer Engineering, Seoul National University, Seoul 08826, South Korea
[5] CIATEQ, A.C. Centro de Tecnología Avanzada, Queretaro 76150, Mexico

Corresponding author: Sadia Basar (sadiaa.khancs@gmail.com)

ABSTRACT The defocus blur concept adds an artistic effect and enables an enhancement in the visualization of image scenery. Moreover, some specialized computer vision fields, such as object recognition or scene restoration enhancement, might need to perform segmentation to separate the blurred and non-blurred regions in partially blurred images. This study proposes a sharpness measure comprised of a Local Binary Pattern (LBP) descriptor and Pulse Coupled Neural Network (PCNN) component used to implement a robust approach for segmenting in-focus regions from out of focus sections in the scene. The proposed approach is very robust in the sense that the parameters of the model can be modified to accommodate different settings. The presented metric exploits the fact that, in general, local patches of the image in blurry regions have less prominent LBP descriptors than non-blurry regions. The proposed approach combines this sharpness measure with the PCNN algorithm; the images are segmented along with clear regions and edges of segmented objects. The proposed approach has been tested on a dataset comprised of 1000 defocused images with eight state-of-the-art methods. Based on a set of evaluation metrics, i.e., precision, recall, and F1-Measure, the results show that the proposed algorithm outperforms previous works in terms of prominent accuracy and efficiency improvement. The proposed approach also uses other evaluation parameters, i.e., Accuracy, Matthews Correlation Coefficient (MCC), Dice Similarity Coefficient (DSC), and Specificity, to assess better the results obtained by our proposal. Moreover, we adopted a fuzzy logic ranking scheme inspired by the Evaluation Based on Distance from Average Solution (EDAS) technique to interpret the defocus segmentation integrity. The experimental outputs illustrate that the proposed approach outperforms the referenced methods by optimizing the segmentation quality and reducing the computational complexity.

INDEX TERMS Defocus image, segmentation, blurred region, non-blurred region, PCNN, LBP, fuzzy logic, EDAS method.

I. INTRODUCTION

In optical imaging system, out of focus in a digital image is the result of the defocused blur region. In the formation process of optical images, the radiation of light from an optical point on the focal plane is drawn on the sensor's optical point. However, the incoming light from an optical point outside the focal plane illuminates a region's non-optical point on a sensor is called the circle of confusion (CoC). The CoC determines the sharpness of the region in photography. If the CoC is large enough that our eyes can observe it, then defocus

blur will arise. It is worth mentioning that the CoC diameter increases gradually with either shallower or deeper distances from the critical focused spot to the point. The image spot appears focused if the human eye's resolution is more significant than CoC's diameter.

Nowadays, photographers increasingly emphasize defocused images given that these images implicitly are segmented into two parts, i.e., focused or sharp, and out of focus or blurred regions. The blurriness in images is spatially fixed in existing image de-blurring techniques. In defocused images, the lower the distance, the sharper the image features mean, the in-focus region is the foreground, while the background is the out of focus region [1], [2]. However, the blurred

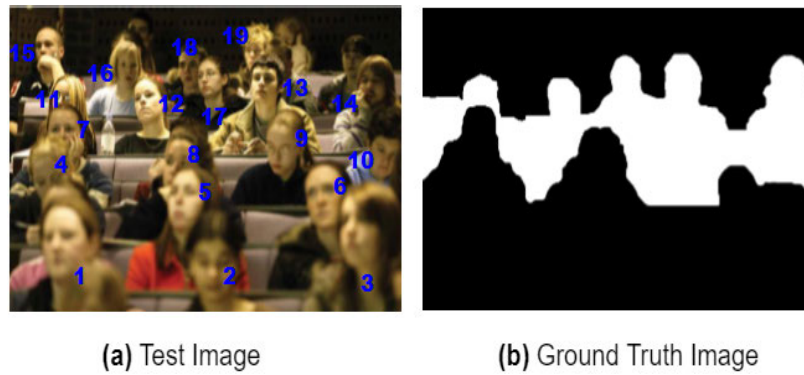The associate editor coordinating the review of this manuscript and approving it for publication was Senthil Kumar [ID].

(a) Test Image   **(b)** Ground Truth Image

FIGURE 1. In the test image, the sharp and blurred objects are identified numerically: the sharp objects are 11, 12, 13 and 14 respectively. The rest of the objects are blurred. In the ground truth image, black denotes the blurred region while white the sharp region.

background can remove details useful for scene understanding purposes. In this case, the focus and out-of-focus regions need to be separated to apply post-processing operations that will affect the focus regions or feature extraction of digital images from in-focus regions.

Some recent image defocuses studies assume that the blurred image results from spatially invariant defocus blur [3]–[8]. The techniques that model the spatially invariant defocus blur usually restore small patches of the image in which the blurred image may preserve the spatial invariant while the restored image patches are collectively stitched [9]–[11]. An accurate and efficient detection of the focused and out of focus regions is vital on various perspectives: a) to avoid costly post-processing tasks such as deconvolution (defocused region) [11]; b) to detect the blurred background in digital imaging comprising image refocusing and de-blurring, estimation of image depth and analysis of the image quality. Also, it can be further deployed for adding a blur effect (i.e., artistic-bokeh effect [15], [16]), specifically for a high DOF mobile camera; c) to detect the blurred objects to extract the image features, and also the spatial pooling of object-centric is performed for detecting the foreground objects in blurred background; d) to recognize the object in the areas wherever the object of interest is out of focus, i.e., microscopy images [38].

The major aim of defocus blur segmentation is to separate sharp and blurred regions for facilitating the post-processing mentioned above tasks. This explicit research problem is adopted herewith; a novel and hybrid approach based on Pulse Coupled Neural Network (PCNN) and Local Binary Patterns (LBP) are presented. The proposed approach achieves promising results, producing smooth edges and object shapes, even in noisy and blurred background images compared to the reference algorithms [45]–[50], [62] which are discussed in detail in the next section. For example, Fig.1 depicts certain focused regions and displays out of focused patches which are numerically identified in the test image.

In the test image, the sharp and blurred objects are identified numerically: the sharp objects are labeled 11, 12, 13, and 14, respectively. The rest of the objects are blurred. In the

ground-truth image, black represents the blurred region, while white spots represent sharp regions.

The fuzzy technique has been applied for various methods used for defocus blur image segmentation. The primary motivation of the prominence of fuzzy-based image segmentation is its extensive functions in various fields, i.e., fuzzy-set theory, supplier segmentation [63], genetic-based schemes, neural networks, computer vision, pattern recognition, and image processing [64]. EDAS is a scheme of fuzzy-logic (FL) proposed by Ghorabaee *et al.* [65], known as Evaluation Based on Distance from Average Solution (EDAS). It is a novel method of the Multiple Criteria Decision-making Method (MCDM) that is used for inventory classification [66]. The FL's EDAS technique is used in the algorithm's ranking to classify the top potential scheme based on execution time, speed, and accuracy.

A. CONTRIBUTIONS

This paper proposes a novel, efficient and accurate approach based on a sharpness metric called Local Binary Patterns (LBP) and a pulse-synchronous mechanism known as Pulse Coupled Neural Network (PCNN) for resolving the defocus blur segmentation problem. Furthermore, the positive threshold values are required in the region extraction process without the requirement of any tuning procedure. The defocused regions are entirely extracted from the focused ones using the LBP sharpness mask by measuring the blur estimation in defocus images. After extraction, the neuron firing sequence in the PCNN algorithm comprises the image feature details containing the texture, region, and edge are adopted for a prominent segmentation of focused region based on image features. The proposed approach yields significantly accurate results in less computational time and working for the numerous defocus conditions, as noticeable from our experimental defocus segmentation results.

B. PAPER ORGANIZATION

The paper structure is organized as follows: Section 2 presents related works about LDOF images and the PCNN model, followed by LBP and EDAS schemes. The proposed procedure

and its implementation steps are discussed in Section 3. Section 4 discusses the evaluation of experimental results achieved from the proposed approach and explains the dataset and comparison with the state-of-the-art techniques. Lastly, the conclusion of the proposed approach is described in Section 5.

II. RELATED WORKS

This section is divided into two sub-sections. At first, the introduction about LDOF images is provided along with the previous literature of the PCNN. Next, comprehensive related work is presented, covering the LBP-based algorithms followed by the EDAS scheme in numerous application areas.

A. DEFOCUSED IMAGE SEGMENTATION AND PCNN ALGORITHM

This section introduces Low Depth of Field (LDOF) images followed by the PCNN and LBP measurements. The depth of field (DOF) is a metric that depends on the distance between the camera lens, frontal, and posterior angles of the object, which in turn to be sharp [17]. In LDOF images, the lower the distance, the sharper the image features mean the object of interest is focused. However, the out of focus region could be a large area of background, resulting in a loss of detail at large distances [2]. Some standard methods for detecting the object of interest in LDOF images in the literature are edge-based, region detection approaches, and feature transformations. In [18], [19], an edge-based detection method is used to detect the artificial object and analyze the object's contour by measuring the defocused pixels. Conversely, the region-based segmentation is essential in detecting objects in natural images [2], [20]–[22], [76] that explores a region by using high-frequency mechanisms. For example, recent works [23]–[25] use a higher-order statistics (HOS) map from defocused images to highlight the focused regions. A multi-scale fuzzy model is used by Mei *et al.* [26] for identifying the region of interest, whereas the segmentation of the focused region is carried out by using a mixed-energy function. Similarly, Shaik *et al.* [73] introduced a multi-scale re-blurring technique for the detection of the focused region in the saliency space and aimed at curve evolution using LDOF images. Roy and Mukhopadhyay [74] proposed a multi-focus region-based color image fusion that extracts the focused edges from the input image to obtain a better focused fusion image. They adopted Zero-cross and Canny edge detector operators for focused edge extractions. In contrast with approaches that use edge-based or region-based detection methods, the feature-based transform segmentation of LDOF images produces accurate outputs along with some improvements in terms of performance. However, a high computational cost is required to extract the focused object of a single LDOF image. Likewise, Wen *et al.* [75] adopted a two-channel convolutional neural network (CNN) for extracting the clarity map of input fusion images. The morphological filtering is applied for smoothing the clarity map. Finally,

the clear segments of input images are merged for constructing the resultant fused image.

Nevertheless, inspired by the feature transform segmentation method for LDOF images, we turned our attention to PCNN and LBP-based schemes to extract the focused region of LDOF images. There is no training requirement of PCNN (pulse coupled neural network) like other neural-network models. PCNN has some familiar image processing characteristics, for example, global-coupling and pulse-synchronization [59].

PCNN was proposed as a means for tackling complex problems using a bio-inspired parallel processing paradigm. Eckhorn *et al.* [27] proposed this PCNN approach as a new concept in artificial neural networks research, and the origin of its phenomena is the visual neurons of mammalian for provision of synchronization pulses. The PCNN is one layer, and the 2-D array of lattice connected neurons along with a 1-to-1 pixel neuron correspondence such that each neuron is linked with a unique pixel and vice versa [61]. The original implementation of the PCNN model sought to replicate the pulse-burst phenomenon in the visual cortex nervous structure of *cat*. It can be used in various computer vision tasks such as image processing, image segmentation, object recognition, pattern recognition and isolation, image fusion, and enhancement [2]. The PCNN model's excellent properties have recently been used to develop novel algorithms for image segmentation and explore the dynamic synchronization potentials of neural behavior, containing capture activity, synchronization pulse release, automatic signal, and nonlinear module. The PCNN might represent an impressive contribution to image segmentation research in medical, natural, and some other types of images [60], and therefore, we are interested in assessing its strengths and limitations.

However, more thorough research about the application of PCNN for image segmentation is needed to evaluate its applicability and set adequate model parameters. In this sense, Deng and Yi-De [28] were the first to evaluate the mathematical properties of the PCNN model. Afterward [29], [30], the analysis of the time-attenuation parameters was studied. Kuntimad and Ranganath [31] introduced a scheme for setting the connection-coefficient parameters. An adaptive technique for the parameters' settings to simplify the neuron model was proposed by Chen *et al.* [32]. Yi-De *et al.* [33] and Min and Chai [34] presented the mutual information and Fisher criteria for performance improvement of PCNN in the application of image segmentation. Helmy and El-Taweel [35], Xu *et al.* [36] and Hernández and Gómez [37] proposed a differential-evolution and a self-organizing neural network scheme, respectively, in order to improve the adaptability nature of Pulse Coupled Neural Network (PCNN) for image segmentation applications.

In the context of our work, Shen *et al.* [38] proposed using PCNN for region detection in refocusing images. The refocusing images are suitable for calculating the distance and depth, which uses focused region detection in *3D* measurements. The neuron-firing system extracts the refocused image

features, i.e., edges, texture, and focused region. The major limitation of the presented method is that it is only applicable for light field images.

The spatial characteristics of pixels are considered while applying the PCNN algorithm in image segmentation. (i.e., differences occurring in gray pixel values such as edge discontinuities). The PCNN algorithm's applications are commonly recognized in the industry because the result of its pulse sequence output contains significant information about the textures, edges, and smooth regions in the image [7].

Our proposal utilizes the PCNN algorithm's advantage to transform edge and region features into pulse-sequence images and extract the sharp region of the defocused images from the pulse sequence.

In optics, the image defocuses regions into three types, i.e., sharp, blurred, and transitive. The image features can be mainly classified using texture, color, and shape. The leading role of defocus blur segmentation is to separate the in-focused and out of focused regions in images. A new sharpness metric based on LBP (Local Binary Patterns) and the PCNN model is presented for resolving this issue.

B. LBP BASED SEGMENTATION AND EDAS SCHEME

Ojala *et al.* [39] and Pietikäinen *et al.* [40] proposed one of the popular texture descriptors called Local Binary Pattern (LBP). LBP measures the differences in the pixel values between the central and neighboring points to create a binary descriptor. That binary pattern produces a decimal value that is applied for labeling a certain pixel. Formally, it is explained that for a certain pixel x_c, the LBP calculation is compared with the neighboring pixels $\{x_{p,r}\}_{m=0}^{p-1}$, on a circular radius r on x_c centroid.

Yi and Eramian [62] described LBP pattern-based defocus blur segmentation which separates the focus and out of focus regions in LDOF images. The suggested method makes blurry regions having significantly less prominent in the LBP descriptor than in sharp regions. A quality sharpness map can be produced by merging the presented method and image multi-scale and matting inference.

LBP is commonly used in image analysis and computer vision applications due to its low computational complexity requirements and simple implementation. LBP has been extensively used for texture analysis; its applications have been extended to other diverse categories, for example, remote sensing area, image retrieval, visual object inspection, bio-metric image analysis (face image and fingerprint recognition), edge detection, object motion analysis, environmental modeling, and texture recognition [41]- [43]. LBP invariants have been developed to improve its discriminating power, applicability, and reliability. The LBP function presented by [44] for a given pixel is explained in Eq. (1) and Eq. (2) as below:

$$LBP_{p,r}(y_c) = \sum_{m=0}^{p-1} s(y_{p,r,m} - y_c)2^m \quad (1)$$

$$s(x) = \begin{cases} 1 & x >= 0, \\ 0 & x < 0 \end{cases} \quad (2)$$

where y_c denotes the central pixel value, y_p ($p = 0, \cdots, p-1$) characterizes the neighboring pixels value on a circle-of-radius r and the neighboring pixels denoted by p. The gray level neighboring pixels y_p that do not fall in the central pixels can be estimated by first-order hold interpolation.

The enhancement of image rotation in terms of achievement to rotation invariant $LBP_{p,r}^{ri}$ version [44] as suggested in Eq. (3) as follows:

$$LBP_{p,r}^{ri} = \min \{ROR(LBP_{p,r}, i) \mid i = 0, \cdots, p-1\} \quad (3)$$

where $ROR(x, i)$ denotes an i-step circular bit-wise right shift on x vector.

Shi *et al.* [45] presented the uniform patterns as basic texture micro-structures and it is represented by 'U' values investigated bitwise changes appeared in the LBP pattern which is illustrated in Eq. (4) as given below:

$$U(LBP_{p,r}) = \sum_{m=0}^{p-1} s(y_p - y_c) - s(y_{p-1} - y_c) + \mid s(y_{p-1} - y_c) - s(y_0 - y_c) \mid \quad (4)$$

The bitwise transition is calculated by $U(LBP_{p,r})$ from $0 - 1$ and $1 - 0$. The LBP descriptor is uniform if $U <= 2$ or otherwise is categorized as a non-uniform pattern. The uniform pattern is further classified into $p + 1$ various rotation invariant classification in terms of the rotation-invariant uniform pattern known as

$LBP_{p,r}^{riu2}$ with a lower pattern dimensionality of $p + 2$, identified in Eq. (5).

$$LBP_{p,r}^{riu2} = \begin{cases} \sum_{m=0}^{p-1} s(y_p - y_c), & if \ U(LBP_{p,r}) <= 2 \\ p + 1, & \text{otherwise.} \end{cases} \quad (5)$$

Shi *et al.* [45] proposed a scheme for the estimation of just noticeable blur in images with a new sparse feature based on earlier feature schemes. The presented results illustrated a strong correlation between the extracted features with the defocus strength. The authors presented several possible application areas of the trained features, including image refocus, image de-blurring, and depth estimation.

The above-presented framework's primary limitation is that it suffers heavily under noise and mixes the image and noise content when constructing the descriptor. Therefore, the LBP code has an undefined state and determines the consistent bit value based on another LBP code bit that might be worth deriving the explicit treating of noise detection of the blur region required. The future aim of the authors' work is to compensate for the blur map in the areas of image detection and classification.

Vu *et al.* [46] suggested an algorithm known as S_3 which measures the perceived-sharpness in defocused images. The proposed S_3 approach, along with spatial S_1 and spectral S_2

TABLE 1. Fuzzy logic EDAS's impact in related research studies.

Author(s)	Title of research	Method description
Basar *et al.*[67]	"Unsupervised color image segmentation: A case of RGB histogram-based K-means clustering initialization"	Developed K-means initialization for solving the problems of unsupervised image segmentation using the EDAS method.
Ilieva *et al.*[68]	"Decision analysis with classic and fuzzy EDAS Modifications"	Proposed the L1 parameter in EDAS technique for resolving certain issues in MCDM problems to reduce time complexity.
Liang *et al.*[69]	"An Integrated EDAS-ELECTRE Method with Picture Fuzzy Information for Cleaner Production Evaluation in Gold Mines"	Presented a scheme for 4 level degrees of membership with PFNs(picture fuzzy numbers) to evaluate the production of cleaner in gold mines.
Li *et al.* [70]	"Linguistic-Neutrosophic Multi-criteria Group Decision-MakingApproach with EDAS technique"	The suggested technique introduced the MCGDM (Multi-criteria GroupDecision-Making) approach based on the EDAS for fixing and managing collective neutrosophic issues.
Stevic *et al.*[71]	"Evaluation of Suppliers Under Uncertainty: A Multiphase ApproachBased on Fuzzy AHP and Fuzzy EDAS"	The Fuzzy Analytic Hierarchy scheme is presented to choose and assess the suppliers and aimed at the exploration of the Fuzzy based EDAS scheme."
Mehmood *et al.* [72]	"A Trust-Based Energy Efficient and Reliable Communication Scheme (Trust-Based ERCS) for Remote Patient Monitoring in Wireless BodyArea Networks"	This proposed approach is aimed at a consistent communication scheme to retain the privacy of WBAN (Wireless Body Area Network) and assessed by EDAS scheme and stated on topmost rank

application domains, is used to analyze the perceived sharpness inside and across the defocus images. The resultant sharpness measure is the geometric mean of the S_1 and S_2 measures. The suggested approach's major limitation is that its accuracy is affected by Gaussian noise applied in defocus images.

Shi *et al.* [47] presented a method based on blur features. Various blur domains are described and combined in a multi-scale module to adjust the scale variance. The authors produced the LDOF dataset and ground truth images that will be used in future research directions. The main limitation of the presented method is that its performance sometimes degrades when texture-less background or motion-blurred foregrounds are present, and the blur pixels are identified in these types of regions.

Su *et al.* [48] presented a scheme for detection and classification of blur region in the image that adaptively detects and classifies the types of blur regions regardless of using kernel or de-blurring estimation. A novel singular-value feature is used for the detection of the blurred region within the image. The suggested scheme uses the alpha channel's information to classify the blur type (i.e., motion blur or defocus blur regions). One of the shortcomings of the presented method is that the whole image's blurriness degrades the blur degree estimation quality as the analysis is performed by

singular-value $\beta 1$. Another aspect of performance affected is the proportion regarding the domain size of blurriness to the size of the entire image.

Zhuo and Sim [49] proposed a new technique for blur map amount estimation at edge points using the Gaussian ratio algorithm. The estimation of the depth map is another concept applied for defocus blur segmentation. The defocus map can be assessed twofold: one is for assessing the blur amount at edges, and another is for blur measurement for the rest of the image. A complete defocus map can be generated by applying the interpolation technique. The proposed result is not affected by noise or spurious edge points, and thus it generates more robust defocus maps than earlier studies. The proposed technique applies the size of the edge as a ground reference for depth estimation under the notion that the blurred region edges are large compared to sharp regions. The proposed study's future direction is to compensate for the application in the motion blur domain and work in other edge estimation of digital images.

Zhu *et al.* [50] estimated the point spread functions (PSF) for revealing the geometric knowledge of the image scene and recovering the sharp region in the image. The presented algorithm can estimate a defocus map using a single defocus image and work with classical cameras. The proposed method uses the color information about edges for producing

the blur map to identify the blurriness at every pixel level.

The Evaluation Based on Distance from the Average Solution(EDAS) based approaches are adopted to rank alternative methods in this research study. The individual latest researches about the various impacts of the fuzzy logic EDAS approach in numerous areas is given in Table 1.

III. PROPOSED APPROACH

The PCNN model is generated from pulse-coupled neurons, which is an array model of two-dimensional mono-layer neurons [38]. In the PCNN algorithm, the neurons denote the pixels for their application in image segmentation. In the PCNN model, when a neuron (pixel) gets fired, then all pixels of a similar category fire concurrently because the model has a neuron coupling nature. Based on such a coupling nature, the model processes the digital images using multiple techniques.
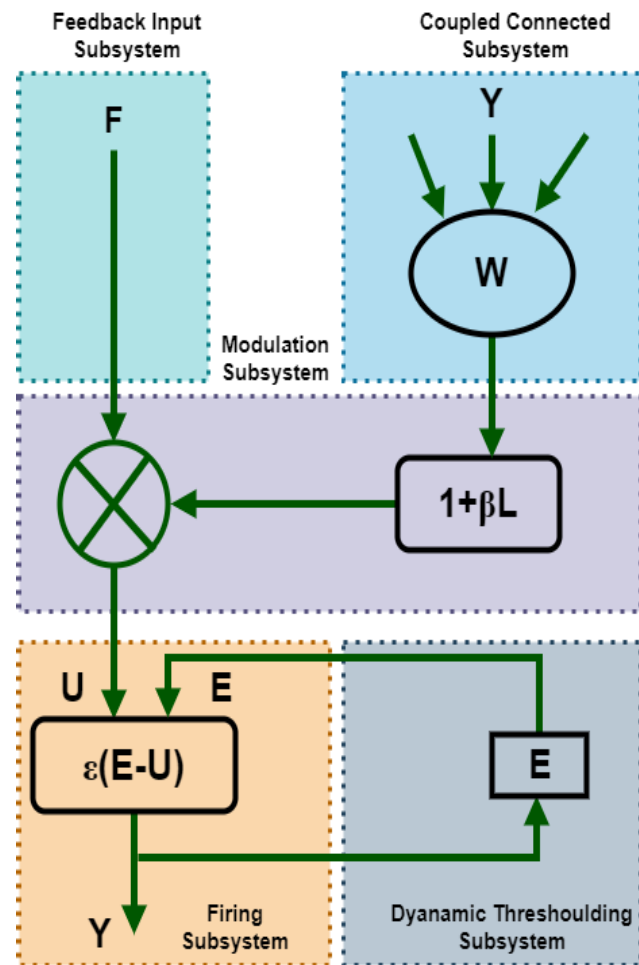

FIGURE 2. Detail structure of PCNN model.

The PCNN model is reported in Fig.2. Each subsystem in the model can be represented by the following mathematical Eq. (6-10):

$$F_{ij}(n) = X_{ij} \tag{6}$$

$$L_{ij}(n) = V_L \sum W_{ijkl} Y_{kl}(n-1) \tag{7}$$

$$U_{ij}(n) = F_{ij}(n)(1 + \beta B L_{ij}(n)) \tag{8}$$

$$E_{ij}(n) = e^{-a_E} E_{ij}(n-1) + V_E Y_{ij}(n-1) \tag{9}$$

$$Y_{ij}(n) = \epsilon [E_{ij}(n) - U_{ij}(n)] \tag{10}$$

Eq. (6) represents the coupled connecting subsystem; the feeding input subsystem is denoted by Eq. (7), Eq. (8), and Eq. (9) characterize the modulation and dynamic thresholding subsystem, whereas the firing subsystem is described by Eq. (10). The gray-scale pixel of the neuron is represented by S_{ij}. The subscript ij denotes the coordinates of the central position of the neuron model. The subscript kl denotes the specific location of the central pixel corresponding to the neighboring pixels, and βB represents the connecting coefficient of the modulation subsystem's internal activity, whereas ϵ represents the dynamic strength coefficient. The representations of a_E and V_E for iteration decay of time constant and connecting weight amplification coefficient in between the dynamic thresholding and the firing subsystem, respectively. The Y_{ij} represents the resultant output of the *PCNN* that is the firing state (0 or 1) of the neuron. The focused region in image segmentation is detected by the natural firing process of neurons or triggered by its neighbor. Each neuron in the model gets fired only once during each iteration. The setting of minimal threshold attenuation is to ensure that all neurons have the opportunity to be fired. All the neurons get fired when the dynamic thresholding is set to be the minimum limit of attenuation. The adjacent pixels' gray level values are estimated by firing the neighboring neurons. Similarly, the neurons firing order reflects the change in the gray values of pixels. We used previous knowledge of neuron firing to estimate the regional characteristics of defocused images. The neurons in PCNN are fired and then act on their neighboring neurons using the connection and feedback subsystems. In the next iteration, the dynamic threshold decay of adjacent neurons gets fired.

The Local Binary Patterns (LBP) descriptor [51] is widely used for texture segmentation [52], face recognition [53], texture recognition [54] and background subtraction [52]. The LBP pixel code at the particular central location is (x_{cen}, y_{cen}) given in Eq. (11) and Eq. (12) as follows:

$$LBP_{N,R}(x_{cen}, y_{cen}) = \sum_{p=0}^{N-1} V(n_p - n_{cen}) \times 2^p \tag{11}$$

$$V(x) = \begin{cases} 1 & |x| >= Th_{LBP} \\ 0 & |x| < Th_{LBP} \end{cases} \tag{12}$$

where n_{cen} is denoted as the central pixel intensity (x_{cen}, y_{cen}), n_p symbolizes the N neighboring pixels intensities that are located within a circle of radius R at central point of circle n_{cen}. It is stated in [55] that $Th_{LBP} > 0$ is a small and positive threshold for obtaining robust image regions. Fig.3 illustrates the neighboring pixel locations n_p for $R = 1$ and $N = 8$. The bilinear interpolation technique is used for obtaining the intensity of the pixels n_p.
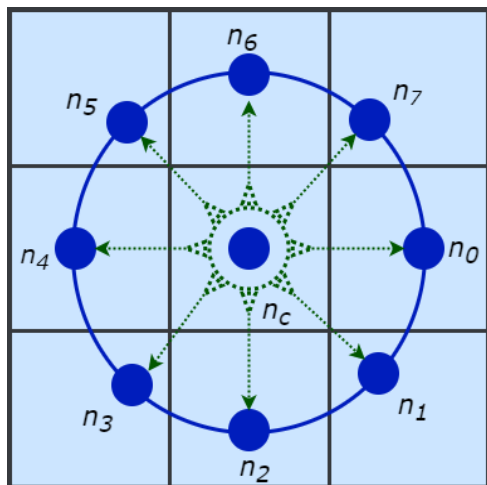
FIGURE 3. 8-bit based LBP along-with P = 8, R = 1.

The rotation-based LBP invariant version is obtained by performing a bitwise right circular shift that minimizes the LBP code result [51]. Consequently, the novel pattern number can be minimized to 36. Ojala *et al.* [51] stated that equal sustenance rotation is not mandatory for rotation invariant patterns. The uniform pattern requires two bits of transitions in a circular sequence, such as one to zero or zero to one. The non-uniform patterns are considered a single pattern, which minimizes the uniform pattern number to 8 in the case of 8-bit LBP, which are depicted in Fig.4. This figure shows the green color of neighboring pixels if it is triggered that is Th_{LBP} is less than their pixel intensity difference and central pixel, else the red colored neighboring pixels will display, which is also explained in Eq. (13).

$$m_{LBP} = 1/N \sum_{j=6}^{9} n(LBP_{8,1}^{rjv2}j) \qquad (13)$$

where $n(LBP_{8,1}^{rjv2}j)$ is the rotation invariant number of uniform 8-bit LBP pattern of type j while N denotes the number of the total pixels in a certain local region and $m_{LBP} \in [0, 1]$. The LBP sharpness measure's major advantage is that it is good for monotonic illumination changes frequently occurring in natural images. Symbols used in this study are illustrated in Table 2.

A. PROPOSED BLUR-SEGMENTATION ALGORITHM
The modules of the proposed approach are discussed in this section. At first, the LBP sharpness mask generation is discussed in detail, while the blur estimation is illustrated as the second module. The third module is all about PCNN model structure, whereas the algorithm description along with Algorithm 1 is reported in the section.

1) LBP SHARPNESS MASK GENERATION
The local binary patterns (LBP) descriptor is produced using m_{LBP}. The sharpness measure is calculated for a local image patch regarding each pixel in the image. The sharp area of the image is displayed as white in Fig.6. The sharpness mask can be calculated using each pixel's constant time for a stable P and R. The image is analyzed based on the LBP sharpness matrix. Then a mask called a sharpness mask is generated using this estimated sharpness matrix. The image is divided into small patches, and the sharpness measure is done on each image patch. This process is done so that the m_{LBP} values of the patch are calculated; then, each patch is categorized either as blur or sharp based on this value. After looping through the entire image, patches with sharp and blur segments will be generated from the sharpness matrix.

2) BLUR ESTIMATION
Blur estimation is defined as the process of estimating the blurred content in the image. Using LBP, the pixels with sharp values and those with blur values are identified. The blur estimation is done using this pixel information so that the pixels that fall under the blur category are replaced with zero intensity values. This process helps the segmentation to act on individual pixels. Using this estimated blur image, a binary mask corresponding to the segmented image is generated.

Fig.5 illustrates the frequency distribution of 9 uniform patterns of LBP showing focused and out-of-focused regions of 100 images selected randomly from the available public dataset of 1000 partial, blurred natural images [16] along with ground truth images indicating the focused and out-of focused regions. The graph's horizontal axis shows the histogram of local binary patterns, while the number of occurrences indicates the vertical side. The frequency patterns of out-of-focused regions in bins 5, 6, 7, 8, and 9 are visibly less than focused regions. The reason is that in smoother regions, most neighboring pixels have the identical intensity specified to nc. However, in some cases, fewer neighboring pixels are triggered as their LBP patterns are less uniform, along with fewer likely triggered neighbors.

3) PCNN MODEL STRUCTURE
The model PCNN generates promising segmentation results in the case of low contrast and noisy test images. It has been observed that in the case of overlapped adjacent regions, even when the intensity ranges of adjacent regions overlap, the PCNN may produce accurate regions segmentation if certain conditions are satisfied. It is noted that when an accurate segmentation has been obtained, each pixel is appropriately allocated to the region it belongs to. The generic technique for image segmentation using PCNN is to adjust the network parameters so that the neurons corresponding to the pixels of a given region pulse together and the neurons corresponding to adjacent regions' pixels are not triggered. The network neurons pulse based on their feeding and linking inputs. Note that the feeding input to a neuron is equal to the intensity of its corresponding pixel. Due to the captured phenomenon, the neurons associated with each group of spatially connected pixels with similar intensities tend to pulse together. The image segmentation process can be identified by the synchronous
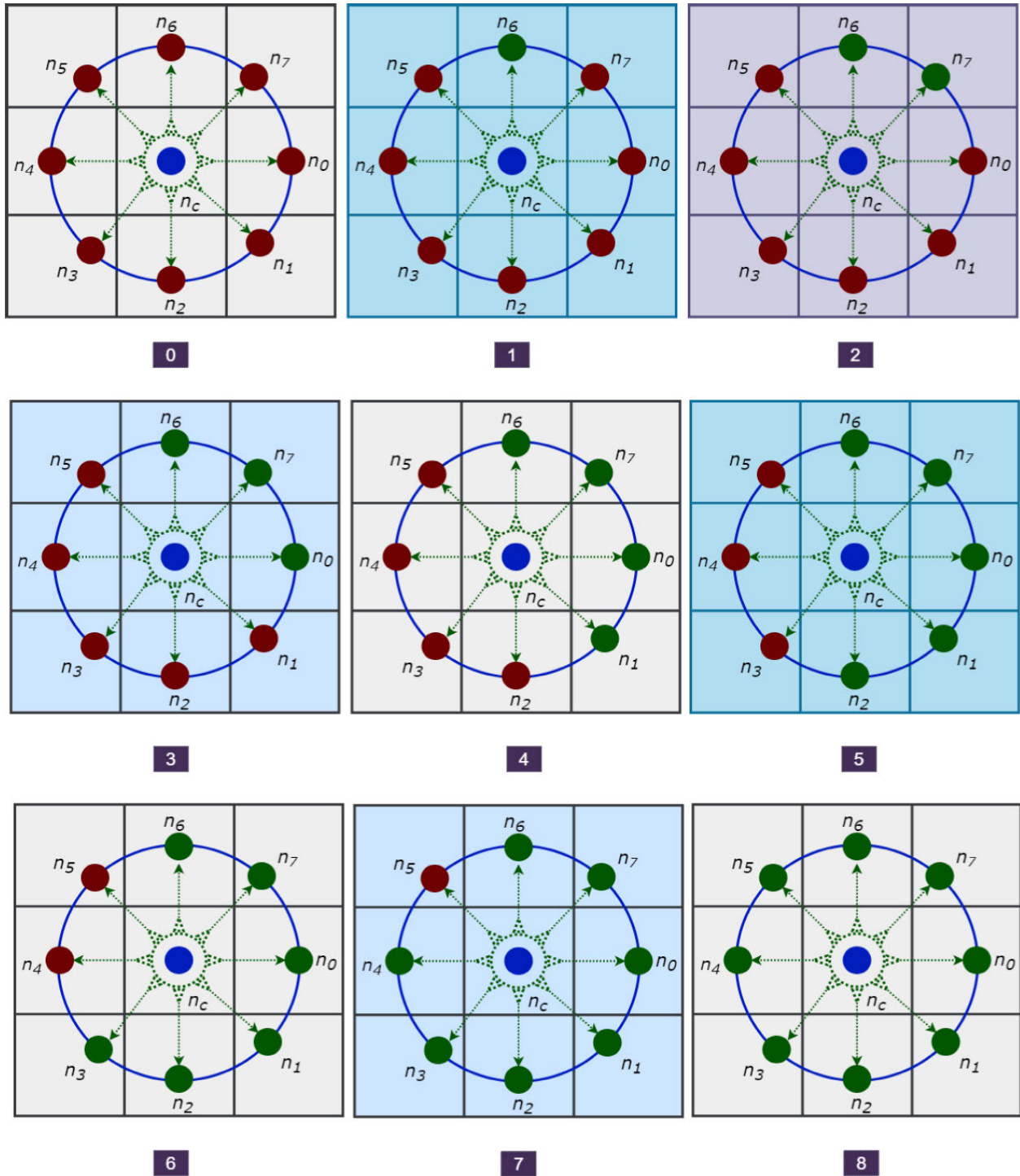
FIGURE 4. The invariant LBP based uniform rotation.

pulsing neurons of each contiguous set. The PCNN based segmentation can be a region, part of a region, or numerous regions, unions, and sub-regions of the test image. Ideally, the goal is to select the network parameters such that each segment exactly corresponds to an entire region in the image. The quality of the attainable segmentation is based on such

parameters. Conversely, the PCNN may not always produce accurate segmentation of real images, and for this reason, further post-processing steps are required for splitting and merging the segments.

In our approach, the input image is converted into a gray-scale, and this image is evaluated in the frequency

TABLE 2. Symbols and descriptions.

Symbol	Description
PCNN	Pulse Coupled Neural Network
LBP	Local Binary Pattern
CoC	Circle of Confusion
ROI	Region of Interest
OOI	Object of Interest
HOS	Higher Order Statistics
LDOF	Low Depth of Field
MCC	Matthew's Correlation Coefficient
JC	Jaccard Coefficient Measure
DSC	Dice Similarity Coefficient
GPU	Graphics Processing Unit
PSF	Point Spread Functions
I_{Def}	Original image
FI_{seg}	Output image
$I_{\text{Gry}_{(Omega)}}$	Gray scale image region
$\text{Max}_{\text{Omega}}$	Maximum frequency region
$\text{Min}_{\text{Omega}}$	Minimum frequency region
$\text{Mean}_{\text{Omega}}$	Average frequency region
$I_{\text{Def}(ij)}$	The pixel coordinate (i, j) in the test image
Th_{LBP}	Threshold *LBP* value
$Is_{(ij)}$	Binary segmentation of *LBP* algorithm
$Edge_{\text{Matrix}}$	Output edge map of PCNN
B	The firing sequence matrix for recording pixel's firing order
W	Linking weight matrix
μ_{LF}	Gray-level mean values of low level frequency
μ_{MF}	Gray-level mean values of mid level frequency
μ_{HF}	Gray-level mean values of high level frequency
β	Linking strength
γ_E	Dynamic threshold amplitude
χ_E	Decay factor
TH_{min}	Threshold with minimum limit
ρ	Judgment-criteria
ω	Dynamic threshold matrix
$\text{Connectivity}_{\text{Matrix}}$	Pixel connectivity-matrix
FB_{seg}	Final segmented binary image
FI_{seg}	initial segmented color image
EDAS	Evaluation Based on Distance from Average Solution

domain to extract the low frequency, medium frequency, and high-frequency regions. The mean of the three frequency regions is then calculated. The PCNN is executed on the gray-scale image using these values as initial parameters. The PCNN algorithm is executed on every pixel in the image; after completing the entire firing sequence, a segmented edge image is generated. This segmented edge image is merged and binarized to obtain the final segmented image, as depicted in Fig.6.

4) ALGORITHM DESCRIPTION
The focused-segmentation algorithm using the proposed hybrid approach is illustrated in Algorithm 1. Our method takes an *LDOF* image as an input and produces visible image regions as an output. The algorithm comprises five major parts: parameters initialization, generation of the matrix for firing sequence, pixels classification, calculation of the LBP descriptor, and assessing the quality of segmentation of the visible regions.

The proposed algorithm requires numerous parameters, i.e., linking weight matrix W, linking strength β, dynamic threshold amplitude γ_E, decay factor χ_E, a threshold with minimum limit TH_{min}, and judgment-criteria ρ. The starting value of W has been calculated experimentally. The other parameters for example γ_E, TH_{min}, χ_E, ρ, and β are adaptively configured as per gray level distribution in the images.

Algorithm 1 Defocus Blur Region Segmentation

Input: Defocused image I_{Def}

Output: Final focused segmented image FI_{Seg}

1) Convert I_{Def} to gray-scale image I_{Gry}
2) $I_{\text{Gry}_{(\text{Omega})}} \leftarrow fft(I_{\text{Gry}})$
3) $Max_{\text{Omega}} \leftarrow max(I_{\text{Gry}_{\text{Omega}}})$
4) $Min_{\text{Omega}} \leftarrow min(I_{\text{Gry}_{\text{Omega}}})$
5) $Mean_{\text{Omega}} \leftarrow mean(I_{\text{Gry}_{\text{Omega}}})$
6) Calculate the *PCNN* initial parameters using initialization formula. (see equations (15) to (28).
7) Estimate the sharpness using the *LBP* sharpness measure formula. (see equation (12))
8) **for** *ij* pixel position in I_{Def} **do**
9)   **if** $I_{Def(ij)} > Th_{LBP}$ **then**
10) $Is_{(ij)} \leftarrow 0$
11)   **else** $Is_{(ij)} \leftarrow I_{Def\ (ij)}$
12)   **end if**
13) **end for**
14) $\text{Edge}_{\text{Matrix}} \leftarrow 0, B \leftarrow 0, \text{Connectivity}_{\text{Matrix}} \leftarrow 0$ and $n \leftarrow 1$
15) **for** *ij* pixel position in *Is* **do**
16)   Calculate $F_{ij}(n), L_{ij}(n), U_{ij}(n), E_{ij}(n), Y_{ij}(n)$.
17)   **if** $Y_{ij(n)} == 0$ **then**
18) $\text{Edge}_{\text{Matrix}(ij)} \leftarrow 1, B_{(ij)} \leftarrow 1$
19)   **else** $\text{Edge}_{\text{Matrix}(ij)} \leftarrow 0, B_{(ij)} \leftarrow 0$
20)   **end if**
21) **end for**
22) **for** *ij* pixel position in *Y* **do**
23)   **if** $Y_{ij} == 1$ **then**
24) $Lb \leftarrow$ bwlabel(Y)
25)   **end if**
26) **end for**
27) **for** *ij* pixel position in $\text{Connectivity}_{\text{Matrix}}$ **do**
28) $\text{Connectivity}_{\text{Matrix}\ (ij)} \leftarrow$ the connectivity of the position *ij* in *Lb*
29) **end for**
30) $n \leftarrow n + 1$
31) **for** *ij* pixel position in $\text{Edge}_{\text{Matrix}}$ **do**
32)   **if** $\text{Edge}_{Matrix(ij)} >$ Threshold
33) $\text{Edge}_{\text{Matrix}(ij)} \leftarrow 1$
34)   **else** $\text{Edge}_{\text{Matrix}(ij)} \leftarrow 0$
35)   **end if**
36) **end for**
37) $FB_{\text{seg}} \leftarrow$ binary$(\text{Edge}_{\text{Matrix}})$
38) **for** *ij* pixel position in *Imc* **do**
39)   **if** $FB_{\text{seg}(ij)} == 1$
40) $FI_{\text{seg}(ij)} \leftarrow FI_{\text{seg}(ij)}$
41)   **else** $FI_{\text{seg}(ij)} \leftarrow 0$
42)   **end if**
43) **end for**

The gray-level intensity information is reflected by the linking weight-matrix *W* and the center neuron transmit this information. The effect of gray-level pixels decreases with the increasing level of distance from the central pixel. Our matrix has been initialized and the synaptic weights are represented in the matrix with constant values as illustrated in Eq. (14) as follows:

$$W(ij) \begin{bmatrix} 0.5 & 1 & 0.5 \\ 1 & 0 & 1 \\ 0.5 & 1 & 0.5 \end{bmatrix} \tag{14}$$

The duration of the firing neuron activation in the PCNN algorithm is modified phase-wise. Tsai and Wang [18] mentions that χ_E changes the numbering and height of each firing phase, whereas γ_E alters the matrix width of each firing phase. For instance, each firing neuron's step narrows down with the χ_E, reduces which subsiding its numerical coupling characteristics, and the network behavior of the pulse delivery is displayed. The algorithm efficiency is affected by the gradual reduction of χ_E, and as a result, the duration of each iteration of the algorithm increases. The neuron parallel to the pixel value and the most considerable normalized gray-scale value ($I_{Def}max$) in the entire image must be fired for the initial iteration duration. Thus, γ_E is usually assigned as $I_{Def}max$. Each neuron needs to fire at a single time to avoid overlapping firing cycles of neurons. The threshold value is set to infinity when the neuron is fired. Consequently, the neuron will not be able to fire again in the algorithm's cycle, as illustrated in Eq. (15). The input defocus image I_{Def} is normalized as the matrix ω. This process is usually called the refractory period of the firing (pulsing in this case) neuron.

$$\gamma_E \leftarrow \max(\omega) \tag{15}$$

The proposed method applies simple pre-processing steps of the images that contain measurements of the gray-level statistical distribution, spatial-level frequency statistics, and gray-scale normalization. The parameters are settled according to the images' pre-processing results to improve the proposed algorithm's adaptability. The parameter *THmin* is identified as the gray level distribution of the entire image. Therefore, the pixel numbers along with gray-scale values in the parameter interval [*THmin*, $1 >= 93\%$] of the pixels in ω are produced in the entire image. Three level-descriptive regions such that low, mid, and high-frequency information are extracted from the image. Each descriptive region is the image block with the highest pixel numbers in the resultant frequency band. The gray-level mean values of low, mid, and high-level frequency are represented as μ_{LF}, μ_{MF}, and μ_{HF}, respectively, along with standard deviations αHF. The algorithm used for defocus images requires to fulfill the following criteria by these parameters: the neurons along with low frequency must be fired at a time; neurons with mid-level frequency fire continuously, and the firing sequence for neurons having the high-level frequency has more significant differences.

The two possible conditions for the low-level frequency region are the firing neuron at $n_1 th$ iteration that corresponds gray level pixel value $\mu_{LF} + \alpha_{LF}$. Subsequently, the firing
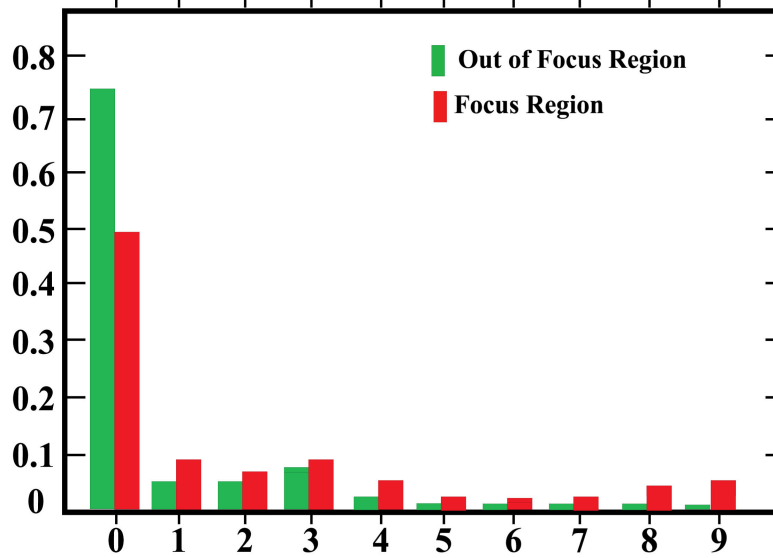
FIGURE 5. LBP histogram in focused and out of focused regions.

neuron at the n_2th iteration that corresponds to gray level pixel value μ_{LF}- α_{LF}. The χ fulfills the below inequality conditions as described in Eq. (16):

$$\mu_{LF} + \alpha_{LF} \geq \gamma_E e^{-(n_1-1)\chi_E} \tag{16}$$

$$\mu_{LF} - \alpha_{LF} \geq \gamma_E e^{-(n_2-1)\chi_E} \tag{17}$$

$$n_2 - n_1 \leq 1 \tag{18}$$

Simplifying the Eq. (16) to Eq. (18), the resultant equation is given by the expression below Eq. (19):

$$\chi_E = ln\frac{(\mu_{LF} + \alpha_{LF})}{(\mu_{LF} - \alpha_{LF})} \tag{19}$$

The assumption about other conditions for the high-level frequency region is the firing neuron at the n_3th iteration that corresponds to gray level pixel value $\mu_{LF} + \alpha_{LF}$. The second firing neuron at the n_{4th} iteration for corresponding gray level pixel $\mu_{LF} - \alpha_{LF}$. The conditions must be fulfilled by the parameters used in Eq. (20) to Eq. (22):

$$\mu_{HF} + \alpha_{HF} \geq \gamma_E e^{-(n_3-1)\chi_E} \tag{20}$$

$$\mu_{HF} - \alpha_{HF} \geq \gamma_E e^{-(n_4-1)\chi_E} \tag{21}$$

$$n_4 - n_3 > \rho \tag{22}$$

Simplifying the Eq. (20) to Eq. (22), the resultant equation is illustrated in Eq. (23):

$$\rho < \frac{1}{\chi_E} ln\frac{(\mu_{HF} + \alpha_{HF})}{(\mu_{HF} - \alpha_{HF})} \tag{23}$$

According to the criteria of classification, the simplification of Eq. (22) and Eq. (23) is givn as follows in Eq. (24) and Eq. (25):

$$0 \leq \rho \leq 8 \tag{24}$$

$$\rho = \min 8\frac{1}{\chi_E} ln\frac{(\mu_{HF} + \alpha_{HF})}{(\mu_{HF} - \alpha_{HF})} \tag{25}$$

The 3×3 neighbor neurons are fired and that is the major reason for neuron firing at the mid-level frequency region. At a time the neurons probably gray-scale μ_M in the 3×3 neighborhood fired in the n_5th iteration. In pulse coupling, these neurons are fired in the n_6th iteration. The simplifications of parameters are given by Eq. (26) to Eq. (28):

$$\mu_M \geq \gamma_E e^{-(n_5-1)\chi_E} \tag{26}$$

$$\mu_M - \frac{2\rho}{3}\beta\mu_M \geq \gamma_E e^{-(n_6-1)\chi_E} \tag{27}$$

$$n_6 - n_5 = 1 \tag{28}$$

Solving Eq. (26) to Eq. (28), the result is given in Eq. (29) as follows:

$$\beta = \frac{3\alpha_{LF}}{\rho(\mu_{LF} - \alpha_{LF})} \tag{29}$$

The parameters $\gamma_E, TH_{min}, chi_E, \rho$, and, β in Algorithm 1 are adaptively assigned as the pre-processing output of the images.

IV. ALGORITHM EVALUATION

We used a blurred detection dataset that is publicly available [16], consisting of 1000 blurred natural images of various categories, i.e., humans, animals, airplanes, ships, trees, beeches, and natural scenes. It must be noted that some of the images present in the dataset are among the most challenging for focus segmentation tasks. Each test image in the defocus dataset has referenced images and one of the best databases for focus segmentation comparisons. The blurred detection dataset is used to analyze the proposed approach because it
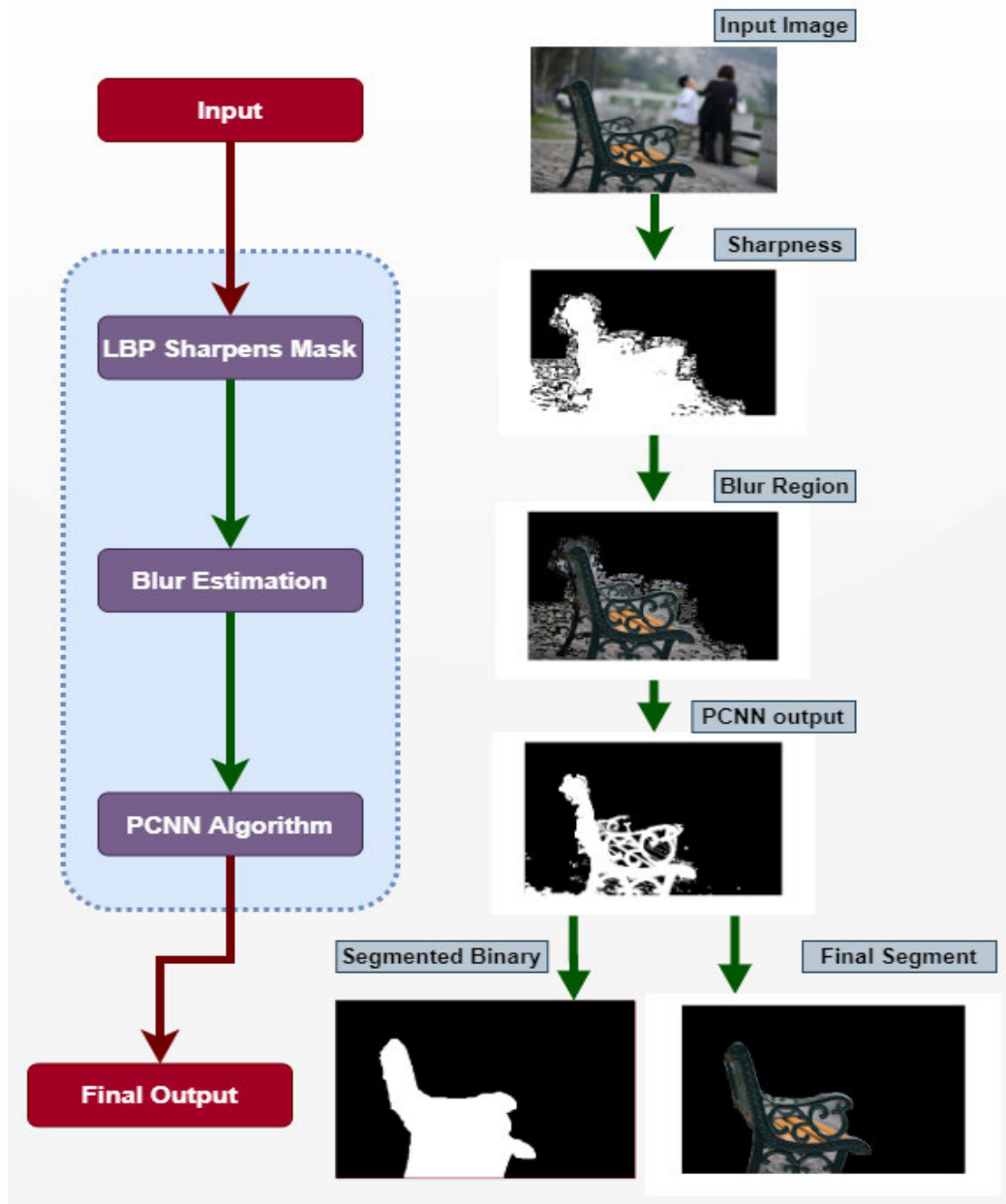
FIGURE 6. The proposed block diagram. The major phases are illustrated on the left while the right depicted each image produced and its role in the algorithm.

contains different classes and several human-generated defocus images. The dataset has been classified into five different sub-classes in this study according to a few specific defocus images for more focus segmentation evaluation.

A. PERFORMANCE METRICS

The proposed approach is compared in this section with other methods in the art for validation purposes. The dataset images were partially segmented into focus and out of focus regions using the method explained in Section IV. The proposed approach for each segmentation algorithm is performed as in Fig.7. The resulting images in Fig.7 are decomposed in black and white colors. The patches corresponding to the sharp region and the blur region in Fig.7 are classified using the proposed hybrid approach. The black color indicates the blur region, while the white color identifies the sharp region. The region corresponding to the blur region is given by the pixel value zero, and the sharp region is given by the value one. In the output, only the sharp objects are noticeable, whereas the blur objects are not visible. In the proposed method, the main errors are attributed, which were the significant limitations of Shi *et al.* [47], Vu *et al.* [46], and Su *et al.* [48] (Section II). The obtained results are very close to the ground truth images with smooth backgrounds,
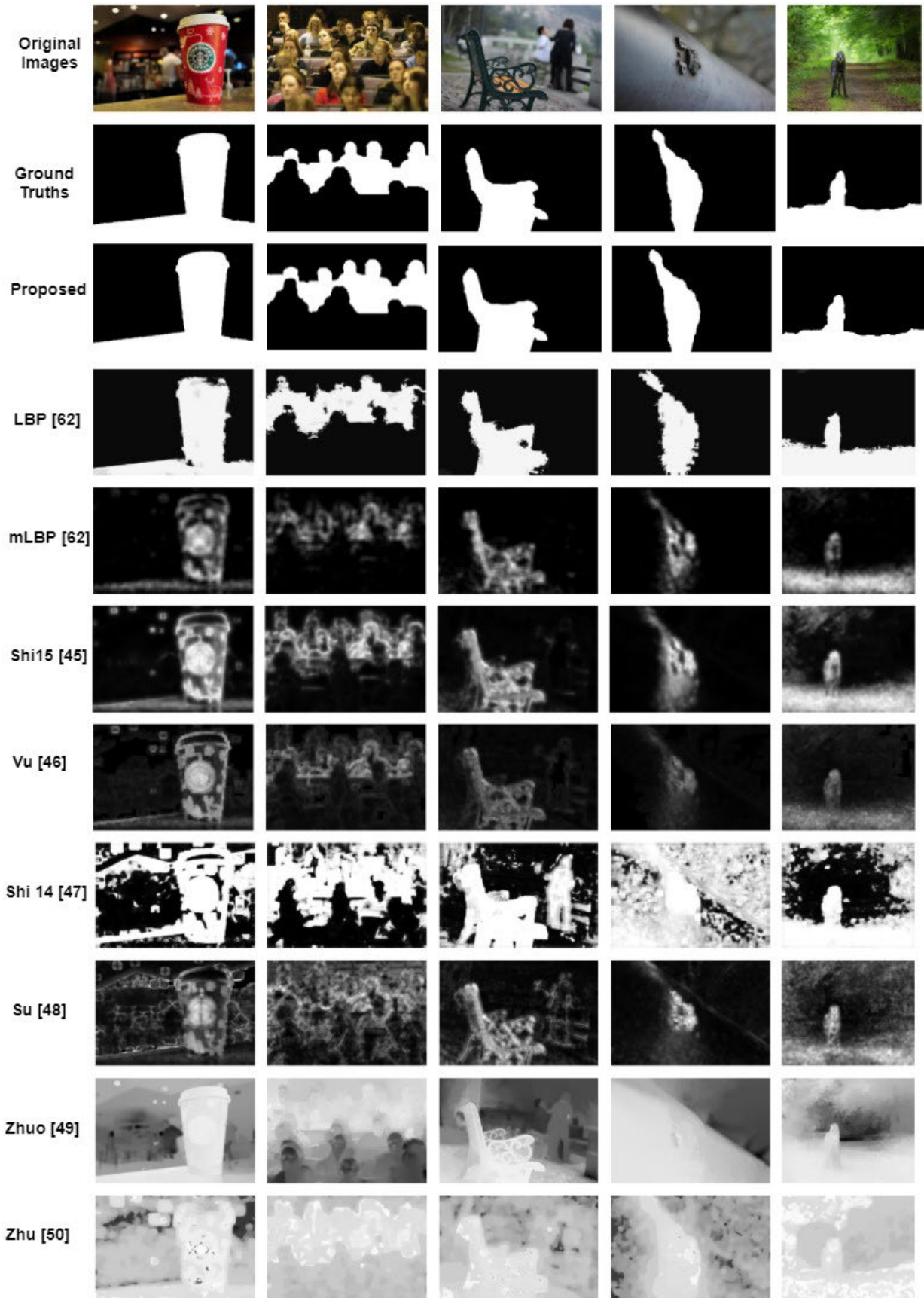
FIGURE 7. Segmentation result performed by numerous blur detection techniques.

while alternate blur detection techniques produce noisy backgrounds. In Shi *et al.* [47], Su *et al.* [48], and Zhu *et al.* [50], one cannot differentiate between the sharp and blur regions as both categories of regions are mixed up and the objects are not properly visible in the output images. Thus, the proposed method is more robust to differentiate the blur backgrounds than previous algorithms.

The proposed method is compared with seven state-of-the-art methods which were concisely discussed in Section II. Yi and Eramian [62] measured the sharpness metric m_{LBP} along with Th_{LBP}. The m_{SVD} was used by Su *et al.* [48] for computing the sharpness map. Vu *et al.* [46] merged the both spectral S_1 and spatial sharpness S_2 by applying the geometric mean method. Shi *et al.* [47] applied the techniques such that m_{GHS}, m_K, m_{LDA}, m_{APS} collectively along with a multi-scale inference model and Naïve Bayes classifier. Shi *et al.* [45] designed a sparse type representation of image patches applying a trained dictionary for minor perceivable blur detection. Zhuo and Sim [49] calculated an edge width based depth map. Zhu *et al.* [50] analyzed the statistical model-based PSF of the local frequency-spectrum of the gradient field.

These techniques' full results are gray-scale images where the more incredible sharpness indicates the greater intensity and other methods except for Zhu and the proposed approach applied the simple thresholding segmentation, T_{seg}, in the final step for generating the segmentation. The parameters in the reference algorithms were used in their original implementation code. Meanwhile, getting the original code for Zhu's method was impossible because it is affiliated with Adobe Systems Inc. Our algorithmic implementation produced all the output results illustrated in this study. The sharpness map was normalized by using the interval [0,8]. In the literature, only three performance metrics, i.e., Precision, Recall, and F-measure, are used to evaluate the blur segmentation algorithm. These three matrices are also used for evaluating the proposed approach along with the referenced methods, besides some other additional metrics, i.e., accuracy, Matthew's Correlation Coefficient (MCC), Jaccard Coefficient Measure (JC), Dice Similarity Coefficient (DSC), and Specificity are also used in this study and was not used in previous techniques. The performance metrics are given as follows:

1) PRECISION AND RECALL
Precision and recall are produced for deblurring the segmentation algorithm to change the threshold Th_{seg} using the interval [0, 255] for generating the final segmentation of the sharpness metric in Eq. (30) and Eq. (31).

$$\text{Precision} = \frac{R_{seg} \cap R_{gtr}}{R_{seg}} \quad (30)$$

$$\text{Recall} = \frac{(R_{seg} \cap R_{gtr})}{R_{gtr}} \quad (31)$$

where R_{seg} denotes the pixels in the blurred segmented region, R_{gtr} identifies the pixels in the blurred ground truth region. The resultant output of precision is 0.9784 while Recall is 1.

The proposed approach produced remarkable precision compared to the existing methods, and the presented approach also generated the enhanced output compared to the LBP method.

2) ACCURACY
The accuracy is calculated from the error matrix, and they are determined by distributing the complete quantity, which properly categorized pixels by the whole quantity of reference pixels. Similarly, the accuracy of distinct groups is calculated by a different number which is properly classified pixels in each column. Accuracy indicates the training set pixel of a given cover type, classified and determined by dividing the number of properly categorized pixels in each group by several training data set, and it is used in the different classes. Accuracy presents the systematic errors, and the precision is related to the random errors. True positive(TP) indicates its segmented output is one and the ground truth results are also one, and true negative (TN) values mean the segmented, as well as the ground truth both, are 0. False-positive (FP) means the segmented result is one while the ground truth result is 0. In contrast, false-negative (FN) leads to a segmentation result is one, whereas the ground truth result is one, and these terms are used to measure the accuracy, and it also measures the total number (N) of cases. The resultant outcome of the accuracy is 0.9964. which is depicted in Fig.10. The retrieved proportion result is defined in Eq. (32) as follows:

$$\text{Accuracy} = \frac{TP + TN}{TP + TN + FP + FN} \quad (32)$$

3) F1-MEASURE
The adaptive threshold approach [56] for deblur segmentation along with the threshold given in Eq. (33) as follows:

$$Th_{seg} = \frac{2}{(Y.H)} \sum_{(u=1)}^{Y} \sum_{(v=1)}^{H} S_{map}(u, v) \quad (33)$$

where Y and H are symbolized as the width and height of the sharpness metric S_{map}. As mentioned in [57], the F1-measure is applied for finding the test accuracy. The average value of precision and recall were calculated by F1-score, which is explained in Eq. (34) as follows:

$$F_\alpha = \frac{((1 + \alpha^2) \cdot \text{precision} \cdot \text{recall})}{((\alpha^2) \cdot \text{precision} + \text{recall})} \quad (34)$$

In [57], the α^2 was assigned as 0.3. Zhu *et al.* used the graph cut technique for creating segmentation instead of the thresholding method. The same LBP parameters which are allocated in that paper were also assigned the same values, i.e., $\omega_0 = 1000, \partial_\omega = 0.04, \tau = 2$. However, the PCNN parameters are assigned as: alphabet $W = [0.5, 1, 0.5; 1, 0, 1; 0.5, 1, 0.5], \alpha = 5$, slide window = 110 by 110, neighboring pixels = 3 by 3. The segmented images explained in Fig.7 are reported in Fig.9. The comparison graph is shown in Fig.8 which explains the clear-cut difference of the proposed approach concerning the compared
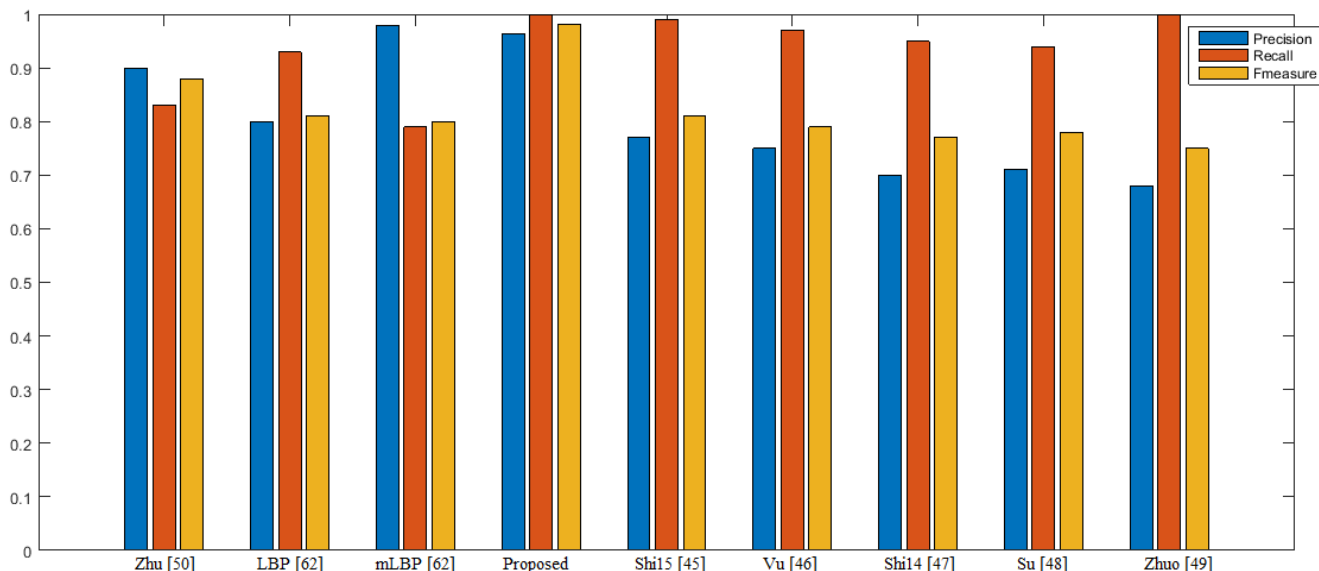
FIGURE 8. Comparative results of Precision, Recall and F-measure for adaptive thresholds. The Zhu result is accomplished by applying graph cut instead of thresholding as mentioned in their paper while *LBP* method result is achieved by using a smaller threshold (i.e., Tseg = 0.3). The proposed approach can achieve comparative performance (precision = 0.9784, recall = 1, F1-score = 0.9891).

FIGURE 9. Binary map segmentation comparison between the proposed approach and Zhu *et al.*.

works. The graph clearly shows that the proposed approach achieves the best results compared to the existing methods: precision = 0.9784, recall = 1, F1-score = 0.9891.

4) MATTHEW's CORRELATION COEFFICIENT (MCC)

MCC is another metric to analyze two binary images' similarity measures, such as the resultant image and ground truth image. Its result ranges between [-1, 1], where -1 denotes the inaccurate result while 1 identifies the accurate output. MCC is considered to be more explainable than the F1 measure and accuracy for binary image evaluation as it takes all four balance ratios of the confusion matrix (TP, TN, FP, and FN). The presented output of MCC is 0.9870 as reported in Fig.10. It can be illustrated in the following Eq. (35).

$$MCC = \frac{((TP) \cdot (TN) - (FP) \cdot (FN))}{\sqrt{([TP + FP][TP + FN][TN + FP][TN + FN])}} \quad (35)$$

where TP indicates True Positive, TN denotes True Negative, FP and FN indicate False Positive and False Negative values, respectively.

5) JACCARD COEFFICIENT MEASURE (JC)

The Jaccard coefficient measure is the opposite of Jaccard distance (JD) that calculates the distance similarity between the two images such as segmented image, and ground truth image is explained in Eq. (36) as below:

$$J(x, y) = \frac{\sum_j \min \ (x_j, y_j)}{\sum_j \max \ (j, y_j)} \quad (36)$$

The *JC* values lies between the interval [0,1] which is illustrated in Fig. 10. The zero value measures the lower similarity while one identifies the higher similarity between the two images.
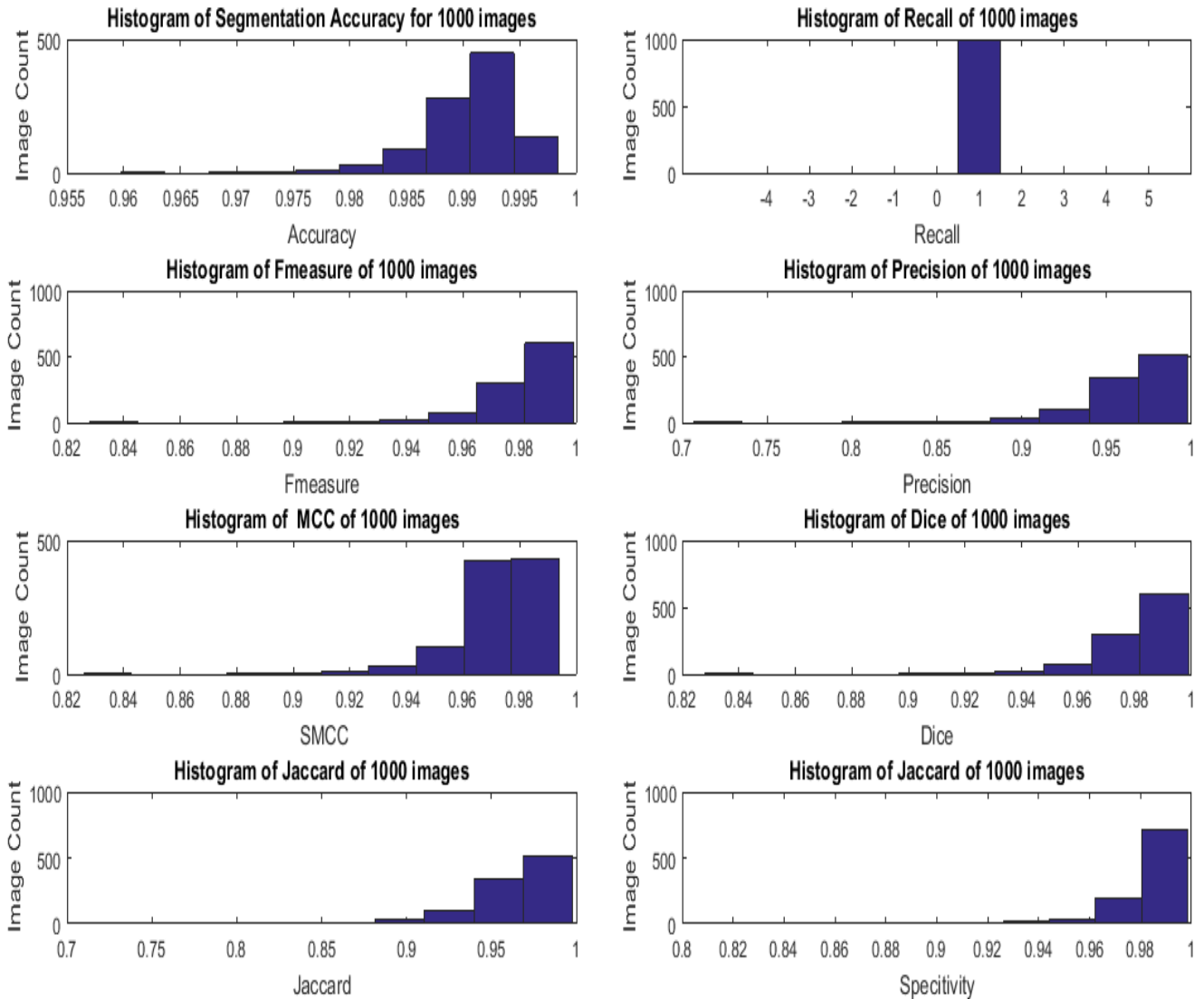
6) DICE SIMILARITY COEFFICIENT (DSC)

As its name implies, DSC is used to measure labeled regions' similarities between two binary images. DSC measure is frequently used in the segmentation process for measuring the performance with efficient weighting instances. These instances are in the range [1, 0]. If the DSC coefficient value is one, this entails an accurate value, whereas a zero value implies a low accuracy. The resultant output of DSC is 0.9891 as shown in Fig.10. It defines in Eq. (37) as follows:

$$DSC = \frac{2TP}{(FP + 2TP + FN)} \qquad (37)$$

7) SPECIFICITY

The expected test evaluates in specific results without displaying an *FP* result denotes the specificity of the numerical value. The expected output of specificity is 0.9957.

The specificity is defined in the following Eq. (38):

$$Specificity = \frac{TN}{(TN + FP)} \qquad (38)$$

The comparative running time of the proposed approach concerning the reference segmentation methods is summarized in Table 3. The proposed approach's running time is spent on the hybrid method (PCNN and LBP) and ranked fourth.

The histogram about different evaluating measures of 1000 datasets is reported in Fig.10. It is worth mentioning that the histogram of all datasets' Recall output value is 1, which indicates a perfect segmentation. Moreover, the histogram output of most images is one or near to 1 in F1-measure, Dice, and specificity, respectively. Furthermore, the histogram output of most of the images of accuracy is near 0.99. Additionally, the precision and Jaccard's output

TABLE 3. Running time comparative analysis of various schemes. The proposed approach is based on *PCNN* and *LBP* methods.

Blur Segmentation Methods	Average Runtime
LBP [62]	27.19 sec
mLBP [62]	40.00 msec
Shi15 [45]	38.36 sec
Vu [46]	19.18 sec
Shi14 [47]	705.2 sec
Su [48]	37.00 sec
Zhuo [49]	20.59 sec
Zhu [50]	12.00 min
Proposed	29.05 sec

TABLE 4. Performance metrics of the various schemes.

Techniques	Performance metrics		
	Precision	Recall	F-Measure
Zhu [50]	0.9632	0.8651	0.8978
LBP [62]	0.8611	0.9651	0.8695
mLBP [62]	0.9871	0.7999	0.8211
Shi15 [45]	0.7651	0.9981	0.8641
Vu [46]	0.7655	0.9772	0.7999
Shi14 [47]	0.6999	0.9651	0.7987
Su [48]	0.7643	0.9644	0.7996
Zhuo [49]	0.6789	1	0.7655
Proposed	0.9784	1	0.9891

of most of the images' histogram is nearly 1. The histogram output of the *MCC* of 1000 images dataset is mostly lying under 0.98 value. It is concluded that the resultant output of mostly metric is almost 1, which proves that the proposed approach created accurate segmentation compared to the existing methods.

B. RANKING BASED EVALUATION OF PERFORMANCE METRICS

In this study, the fuzzy logic-based Evaluation Based on Distance from Average Solution (EDAS) method is used for evaluating the ranking of the proposed approach with reference algorithms in terms of accuracy and possible time complexity reduction. The numerous performance metrics for evaluating the proposed approach are compared with reference methods in this section. In this research, the EDAS method is presented to accumulate cross-efficient outputs of numerous parameters of a total of nine techniques, including ours. The EDAS evaluation in this research is based on three performance metrics only, i.e., Precision, Recall, and F-measure, while the rest of the metrics are only adopted in the proposed approach. The Appraisal Scores (λ) aggregate can be calculated for previous techniques ranking to measure the positive distance from the average solution symbolically represented in the equation as ($P_{\Im}$) and negative distance from the average solution is represented by the symbol ($N_{\Im}$).

In Table 4, the performance metrics are considered the referenced schemes criteria. According to Table 4, the proposed approach and mLBP [62] achieved higher precision than other methods. Likewise, the proposed approach and Zhuo and Sim [49] have the highest Recall, while the high-rank F-measure is reported by the proposed method and Zhu *et al.* [50]. LBP [62], and Zhu *et al.* [50] also record the high precision values, whereas the rest got a lower precision score. The high recall values are achieved by Shi *et al.* [45], and Vu *et al.* [46] compared to other referenced schemes, while the high score F-measure is attained by LBP [62] and Shi *et al.* [45] than previous techniques. Hence, the proposed approach got the best scores of Precision, Recall, and F-measure.

Step 1st: Calculate the solution of the average value (ψ) of all matrices in Eq. (39);

$$(\psi) = [\psi_\beta]_{1 \times \delta} \tag{39}$$

where,

$$(\psi) = \frac{\sum_{i=1}^{x} X_{\alpha\beta}}{x} \tag{40}$$

TABLE 5. Cross-efficient values.

Techniques	Performance metrics		
	Precision	Recall	F-Measure
Zhu [50]	0.9632	0.8651	0.8978
LBP [62]	0.8611	0.9651	0.8695
mLBP [62]	0.9871	0.7999	0.8211
Shi15 [45]	0.7651	0.9981	0.8641
Vu [46]	0.7655	0.9772	0.7999
Shi14 [47]	0.6999	0.9651	0.7987
Su [48]	0.7643	0.9644	0.7996
Zhuo [49]	0.6789	1	0.7655
Proposed	0.9784	1	0.9891
ψ_β	0.82927778	0.948322	0.845033333

Step 1st determines the performance metrics as criteria of numerous approaches. The aggregate calculation of Eq. (39) and Eq. (40) can be obtained as the average value (ψ) for every criterion value calculated as mentioned in Table 5.

Step 2nd: This EDAS step calculates the positive distances from average ($P_{\Im}$) in the Eq. (41), Eq. (42), and Eq. (43) as given below:

$$P_{\Im} = [(P_{\Im})_{\alpha\beta}]_{\delta \times \delta} \tag{41}$$

If the criterion βth is more beneficial then:

$$(P_{\Im})_{\alpha\beta} = \frac{\text{Maximum}(0, \ (A_{V_\beta} - X_{\alpha\beta}))}{A_{V_\beta}} \tag{42}$$

TABLE 6. Analysis results of average ($P_{\jmath}$).

Techniques	Performance metrics		
	Precision	Recall	F-Measure
Zhu [50]	0	0.087757	0
LBP [62]	0	0	0
mLBP [62]	0	0.15651	0.028322354
Shi15 [45]	0.07738996	0	0
Vu [46]	0.07690762	0	0.053410122
Shi14 [47]	0.15601259	0	0.054830184
Su [48]	0.07835466	0	0.053765137
Zhuo [49]	0.18133583	0	0.094118575
Proposed	0	0	0

TABLE 7. Analysis results of average ($N_{\jmath}$).

Techniques	Performance metrics		
	Precision	Recall	F-Measure
Zhu [50]	0.1614926	0	0.062443296
LBP [62]	0.03837342	0.017692	0.028953493
mLBP [62]	0.19031286	0	0
Shi15 [45]	0	0.05249	0.022563212
Vu [46]	0	0.030451	0
Shi14 [47]	0	0.017692	0
Su [48]	0	0.016954	0
Zhuo [49]	0	0.054494	0
Proposed	0.1798218	0.054494	0.170486371

Furthermore, if the criterion is non-beneficial, then the below equation will be changed as follows:

$$(P_{\jmath})_{\alpha\beta} = \frac{\text{Maximum}(0, \ (X_{\alpha\beta} - A_{V_\beta}))}{A_{V_\beta}} \quad (43)$$

The results reflect in Table 6 following as:

Step 3rd: This EDAS step determines negative distances from the average ($N_{\jmath}$) using the Eq. (44), Eq. (45), and Eq. (46) as follows:

$$(N_{\jmath}) = [(N_{\jmath})_{\alpha\beta}]_{\delta \times \delta} \quad (44)$$

If the β_{th} criterion is more beneficial then the following Eq. (45) is:

$$(N_{\jmath})_{\alpha\beta} = \frac{\text{Maximum}(0, \ (A_{V_\beta} - X_{\alpha\beta}))}{A_{V_\beta}} \quad (45)$$

Moreover, if the criterion is non-beneficial, then the given equation will be calculated as follows:

$$(N_{\jmath})_{\alpha\beta} = \frac{\text{Maximum}(0, \ (X_{\alpha\beta} - A_{V_\beta}))}{A_{V_\beta}} \quad (46)$$

where $(P_{\jmath})_{\alpha\beta}$ and $(N_{\jmath})_{\alpha\beta}$ denoted the positive distance and negative distance of β_{th} rated algorithms from the average value concerning α_{th} rating performance parameters, respectively.

The results reflected in Table 7 as given below:

Step 4th: Calculate the aggregate of ($P_{\jmath}$) for the rated algorithms in Table 8 as given below in Eq. (47):

$$(SP_{\jmath})_\alpha = \sum_{\beta=1}^{x} y_\beta (P_{\jmath})_{\alpha\beta} \quad (47)$$

Step 5th: Calculate the aggregate of ($N_{\jmath_{\alpha\beta}}$) for the rated algorithms in Table 9 is as follows in Eq. (48):

$$(SN_{\jmath})_\alpha = \sum_{\beta=1}^{x} y_\beta (N_{\jmath})_{\alpha\beta} \quad (48)$$

The results are reported in Table 9, below:

Step 6th: The scores of $(SP_{\jmath})_\alpha$ and $(SN_{\jmath})_\alpha$ for the rated algorithms as measured and normalizes as given below in the Eq. (49) and Eq. (50):

$$N(SP_{\jmath})_\alpha = \frac{(SP_{\jmath})_\alpha}{\text{maximum}_\alpha((SP_{\jmath})_\alpha)} \quad (49)$$

$$N(SN_{\jmath})_\alpha = 1 - \frac{(SN_{\jmath})_\alpha}{\text{maximum}_\alpha((SN_{\jmath})_\alpha)} \quad (50)$$

Step 7th: This step calculates the score of $N(SP_{\jmath})_\alpha$ and $N(SN_{\jmath})_\alpha$ to get an appraisal-score (AS) which is equal to (λ) for the rated algorithms mentioned in Eq. (51) as below:

$$\lambda_\alpha = \frac{1}{2}(N(SP_{\jmath})_\alpha - N(SP_{\jmath})_\alpha) \quad (51)$$

where $0 \leq \lambda_\alpha \leq 1$.

(λ) is calculated by the aggregate score of NSP_m and NSN_m

Step 8th: Determine the appraisal score (λ) in terms of decreasing order and then measure the ranking of rated algorithms. The best ranking algorithms have the lower (λ). So, in Table 10, the proposed approach has the lowest (λ).

The final ranked result is shown in Table 10 as follows:

The ranking results in Table 10 indicate that the proposed algorithm is on the top rank compared to previous methods.

C. DISCUSSION

The proposed approach may fail in specific images such that noise corrupted images. The problem can be resolved by using some noise-reducing filters before applying the proposed algorithm. The proposed metric was developed by the statistical difference of LBP and PCNN on a partially blurred dataset. Subsequently, the blurriness source is the defocus blur. The proposed metric at present is only able to detect defocus blur. This approach may reduce the segmentation performance in over-exposed images. The over-exposed regions are interpreted as focused regions and which will result in poor segmentation. Furthermore, the concepts adopted in noise-resistant *LBP*(NRLBP) [58], handle those pixels that are susceptible to noise and have an unspecified state. The evaluation section is further improved by adding the EDAS ranking scheme based on three metrics, i.e., Precision,

TABLE 8. Analysis results of the aggregate ($P_\mathfrak{I}$).

Criteria (W)	0.6124871	0.273607	0.113906089	
Techniques	Performance metrics			$(SP_\mathfrak{I})_\alpha$
	Precision	Recall	F-Measure	
Zhu [50]	0	0.024011	0	0.024011
LBP [62]	0	0	0	0
mLBP [62]	0	0.042822	0.003226089	0.046048
Shi15 [45]	0.04740035	0	0	0.0474
Vu [46]	0.04710492	0	0.006083738	0.053189
Shi14 [47]	0.0955557	0	0.006245492	0.101801
Su [48]	0.04799122	0	0.006124177	0.054115
Zhuo [49]	0.11106586	0	0.010720679	0.121787
Proposed	0	0	0	0

TABLE 9. Analysis results of the aggregate ($N_\mathfrak{I}$).

Criteria (W)	0.6124871	0.273607	0.113906089	
Techniques	Performance metrics			$(SN_\mathfrak{I})_\alpha$
	Precision	Recall	F-Measure	
Zhu [50]	0.09891213	0	0.007112672	0.106025
LBP [62]	0.02350322	0.004841	0.003297979	0.031642
mLBP [62]	0.11656417	0	0	0.116564
Shi15 [45]	0	0.014362	0.002570087	0.016932
Vu [46]	0	0.008332	0	0.008332
Shi14 [47]	0	0.004841	0	0
Su [48]	0	0	0	0
Zhuo [49]	0	0.01491	0	0.01491
Proposed	0.11013853	0.01491	0.019419436	0.144468

TABLE 10. Analysis results of 9 referenced schemes.

Techniiques	$(SP_\mathfrak{I})_\alpha$	$(SN_\mathfrak{I})_\alpha$	$N(SP_\mathfrak{I})_\alpha$	$N(SN_\mathfrak{I})_\alpha$	λ_α	Ranking
Zhu [50]	0.024011	0.106025	0.197156455	0.266101	0.231629	**2**
LBP [62]	0	0.031642	0	0.780976	0.390488	**4**
mLBP [62]	0.04604838	0.116564	0.378107311	0.193148	0.285628	**3**
Shi15 [45]	0.04740035	0.016932	0.389208493	0.882799	0.636004	**5**
Vu [46]	0.05318866	0.008332	0.436736788	0.942328	0.689532	**4**
Shi14 [47]	0.10180119	0	0.835898573	1	0.917949	**8**
Su [48]	0.05411539	0	0.444346275	1	0.722173	**7**
Zhuo [49]	0.12178654	0.01491	1	0.896794	0.948397	**9**
Proposed	0	0.144468	0	0	0	**1**

Recall, and F-measure, that declared the proposed approach on top-level rank.

V. CONCLUSION

The proposed approach is based on the PCNN and LBP techniques. The neuron firing sequence comprises the necessary information about image features containing the edge region and texture information soon after detecting the focus region. The suggested method displays the LBP pattern on the focus and out-of-focus regions of the image. The proposed approach has all about the firing sequence of the PCNN model with the design and criterion for pixel classification for creating critical parameters and the sharpness metric-based LBP model. The proposed approach extracts the acceptable regions of images and achieves high accuracy and low computation time compared to state-of-the-art

methods mentioned in the literature review section and a suitable method for defocus blur images. The proposed sharpness metric evaluates the specific LBP patterns in the local neighboring pixels. For more clarification and evaluation, the final outputs of the EDAS ranking technique illustrated that the presented approach is on the top rank, Zhu *et al.* [50], and mLBP [62] on the second and third ranks, respectively, while LBP [62] and Shi *et al.* [45] on the fourth and fifth rank respectively. The algorithms on the seventh and eighth rank are Su *et al.* [48], and Shi *et al.* [47] respectively. The algorithm on the 9th rank is Zhuo and Sim [49]. Henceforth, the complete experimental results and evaluation noticeably report the proposed scheme's outperformance rather than reference schemes in terms of time complexity reduction and possible accuracy in defocus image segmentation.

This research study suggested the focus segmentation of the defocus blur image dataset. Our future direction is to extend the proposed area in medical and 3D image measurement and run on GPU implementation for substantial speed improvement than other defocus segmentation techniques.

REFERENCES

[1] F. Graf, H.-P. Kriegel, and M. Weiler, "Robust image segmentation in low depth of field images," 2013, *arXiv:1302.3900*. [Online]. Available: http://arxiv.org/abs/1302.3900

[2] J. Z. Wang, J. Li, R. M. Gray, and G. Wiederhold, "Unsupervised multiresolution segmentation for images with low depth of field," *IEEE Trans. Pattern Anal. Mach. Intell.*, vol. 23, no. 1, pp. 85–90, Jan. 2001.

[3] R. Fergus, B. Singh, A. Hertzmann, S. T. Roweis, and W. T. Freeman, "Removing camera shake from a single photograph," *ACM Trans. Graph.*, vol. 25, no. 3, pp. 787–794, Jul. 2006, doi: 10.1145/1141911.1141956.

[4] Q. Shan, J. Jia, and A. Agarwala, "High-quality motion deblurring from a single image," *ACM Trans. Graph.*, vol. 27, no. 3, pp. 1–10, Aug. 2008.

[5] D. Krishnan, T. Tay, and R. Fergus, "Blind deconvolution using a normalized sparsity measure," in *Proc. CVPR*, Jun. 2011, pp. 233–240, doi: 10.1109/CVPR.2011.5995521.

[6] A. Levin, Y. Weiss, F. Durand, and W. T. Freeman, "Efficient marginal likelihood optimization in blind deconvolution," in *Proc. CVPR*, Jun. 2011, pp. 2657–2664, doi: 10.1109/CVPR.2011.5995308.

[7] A. Levin, Y. Weiss, F. Durand, and W. T. Freeman, "Understanding and evaluating blind deconvolution algorithms," in *Proc. IEEE Conf. Comput. Vis. Pattern Recognit.*, Jun. 2009, pp. 1964–1971, doi: 10.1109/CVPR.2009.5206815.

[8] D. Krishnan and R. Fergus, "Fast image deconvolution using hyper-Laplacian priors," in *Proc. Adv. Neural Inf. Process. Syst.*, vol. 22, 2009, pp. 1033–1041.

[9] H. Trussell and B. Hunt, "Image restoration of space variant blurs by sectioned methods," in *Proc. IEEE Int. Conf. Acoust., Speech, Signal Process. (ICASSP)*, vol. 3, Apr. 1978, pp. 196–198, doi: 10.1109/ICASSP.1978.1170472.

[10] H.-M. Adorf, "Towards HST restoration with a space-variant PSF, cosmic rays and other missing data," in *The Restoration of HST Images and Spectra-II*. Baltimore, MD, USA: Space Telescope Science Institute, 1994, p. 72.

[11] J. Bardsley, S. Jefferies, J. Nagy, and R. Plemmons, "A computational method for the restoration of images with an unknown, spatially-varying blur," *Opt. Exp.*, vol. 14, no. 5, pp. 1767–1782, 2006.

[12] H. J. Trussell and S. Fogel, "Identification and restoration of spatially variant motion blurs in sequential images," *IEEE Trans. Image Process.*, vol. 1, no. 1, pp. 123–126, Jan. 1992.

[13] D. A. Fish, J. Grochmalicki, and E. R. Pike, "Scanning singular-value-decomposition method for restoration of images with space-variant blur," *J. Opt. Soc. Amer. A, Opt. Image Sci.*, vol. 13, no. 3, pp. 464–469, 1996.

[14] S. Dai and Y. Wu, "Removing partial blur in a single image," in *Proc. IEEE Conf. Comput. Vis. Pattern Recognit.*, Jun. 2009, pp. 2544–2551, doi: 10.1109/CVPR.2009.5206625.

[15] S. Bae and F. Durand, "Defocus magnification," *Comput. Graph. Forum*, vol. 26, no. 3, pp. 571–579, Sep. 2007, doi: 10.1111/j.1467-8659.2007.01080.x.

[16] J. Shi, L. Xu, and J. Jia, "Blur detection dataset," IEEE Comput. Soc., Washington, DC, USA, Tech. Rep., 2014.

[17] A. Adams, *The New Ansel Adams Photography Series: The Print*. New York, NY, USA: Little, Brown and Company, 1980.

[18] D.-M. Tsai and H.-J. Wang, "Segmenting focused objects in complex visual images," *Pattern Recognit. Lett.*, vol. 19, no. 10, pp. 929–940, Aug. 1998.

[19] K. Gai and M. Qiu, "Blend arithmetic operations on tensor-based fully homomorphic encryption over real numbers," *IEEE Trans. Ind. Informat.*, vol. 14, no. 8, pp. 3590–3598, Aug. 2018.

[20] C. S. Won, K. Pyun, and R. M. Gray, "Automatic object segmentation in images with low depth of field," in *Proc. Int. Conf. Image Process.*, vol. 3, 2002, pp. 805–808, doi: 10.1109/ICIP.2002.1039094.

[21] H. Li and K. N. Ngan, "Unsupervized video segmentation with low depth of field," *IEEE Trans. Circuits Syst. Video Technol.*, vol. 17, no. 12, pp. 1742–1751, Dec. 2007.

[22] X.-L. Deng, J.-Q. Ni, Z. Li, and F. Dai, "Foreground extraction from low depth-of-field images based on colour-texture and HOS features," *Acta Automatica Sinica*, vol. 39, no. 6, pp. 846–851, Mar. 2014.

[23] C. Kim, "Segmenting a low-depth-of-field image using morphological filters and region merging," *IEEE Trans. Image Process.*, vol. 14, no. 10, pp. 1503–1511, Oct. 2005.

[24] Z. Liu, W. Li, L. Shen, Z. Han, and Z. Zhang, "Automatic segmentation of focused objects from images with low depth of field," *Pattern Recognit. Lett.*, vol. 31, no. 7, pp. 572–581, May 2010.

[25] S. Ahn and J. Chong, "Segmenting a noisy low-depth-of-field image using adaptive second-order statistics," *IEEE Signal Process. Lett.*, vol. 22, no. 3, pp. 275–278, Mar. 2015.

[26] J. Mei, Y. Si, and H. Gao, "A curve evolution approach for unsupervised segmentation of images with low depth of field," *IEEE Trans. Image Process.*, vol. 22, no. 10, pp. 4086–4095, Oct. 2013.

[27] R. Eckhorn, H. J. Reitboeck, M. Arndt, and P. Dicke, "Feature linking via synchronization among distributed assemblies: Simulations of results from cat visual cortex," *Neural Comput.*, vol. 2, no. 3, pp. 293–307, Sep. 1990.

[28] D. Xiang-Yu and M. A. Yi-De, "PCNN model automatic parameters determination and its modified model," *Acta Electronica Sinica*, vol. 40, no. 5, pp. 955–964, 2012.

[29] D. G. Zhou, C. Gao, and Y. C. Guo, "Adaptive simplified PCNN parameter setting for image segmentation," *Acta Automat. Sinica* vol. 40, no. 6, pp. 1191–1197, 2014.

[30] S. Wei, Q. Hong, and M. Hou, "Automatic image segmentation based on PCNN with adaptive threshold time constant," *Neurocomputing*, vol. 74, no. 9, pp. 1485–1491, Apr. 2011.

[31] G. Kuntimad and H. S. Ranganath, "Perfect image segmentation using pulse coupled neural networks," *IEEE Trans. Neural Netw.*, vol. 10, no. 3, pp. 591–598, May 1999.

[32] Y. Chen, S.-K. Park, Y. Ma, and R. Ala, "A new automatic parameter setting method of a simplified PCNN for image segmentation," *IEEE Trans. Neural Netw.*, vol. 22, no. 6, pp. 880–892, Jun. 2011.

[33] Y.-D. Ma, Q. Liu, and Z.-B. Quan, "Automated image segmentation using improved PCNN model based on cross-entropy," in *Proc. Int. Symp. Intell. Multimedia, Video Speech Process.*, 2004, pp. 743–746.

[34] J. Min and Y. Chai, "A PCNN improved with Fisher criterion for infrared human image segmentation," in *Proc. IEEE Adv. Inf. Technol., Electron. Autom. Control Conf. (IAEAC)*, Dec. 2015, pp. 1101–1105, doi: 10.1109/IAEAC.2015.7428729.

[35] A. K. Helmy and G. S. El-Taweel, "Image segmentation scheme based on SOM–PCNN in frequency domain," *Appl. Soft Comput.*, vol. 40, pp. 405–415, Mar. 2016.

[36] X. Xu, T. Liang, G. Wang, M. Wang, and X. Wang, "Self-adaptive PCNN based on the ACO algorithm and its application on medical image segmentation," *Intell. Autom. Soft Comput.*, vol. 23, no. 2, pp. 303–310, Apr. 2017.

[37] J. Hernández and W. Gómez, "Automatic tuning of the pulse-coupled neural network using differential evolution for image segmentation," in *Proc. Mex. Conf. Pattern Recognit.* Cham, Switzerland: Springer, pp. 157–166, 2016, doi: 10.1007/978-3-319-39393-3_16.

[38] J. Shen, L. Han, M. Xu, C. Huang, Z. Zhang, and H. Wang, "Focused-region segmentation for refocusing images from light fields," *J. Signal Process. Syst.*, vol. 90, nos. 8–9, pp. 1281–1293, Sep. 2018.

[39] T. Ojala, M. Pietikainen, and T. Maenpaa, "Multiresolution gray-scale and rotation invariant texture classification with local binary patterns," *IEEE Trans. Pattern Anal. Mach. Intell.*, vol. 24, no. 7, pp. 971–987, Jul. 2002.

[40] M. Pietikäinen, A. Hadid, G. Zhao, and T. Ahonen, *Computer Vision Using Local Binary Patterns*. vol. 40. London, U.K.: Springer, 2011.

[41] L. Liu, L. Zhao, Y. Long, G. Kuang, and P. Fieguth, "Extended local binary patterns for texture classification," *Image Vis. Comput.*, vol. 30, no. 2, pp. 86–99, Feb. 2012.

[42] X. Qi, R. Xiao, C.-G. Li, Y. Qiao, J. Guo, and X. Tang, "Pairwise rotation invariant Co-occurrence local binary pattern," *IEEE Trans. Pattern Anal. Mach. Intell.*, vol. 36, no. 11, pp. 2199–2213, Nov. 2014.

[43] T. Ojala, M. Pietikäinen, and T. Mäenpää, "Gray scale and rotation invariant texture classification with local binary patterns," in *Proc. Eur. Conf. Comput. Vis.* Berlin, Germany: Springer, 2000, pp. 404–420, doi: 10.1007/3-540-45054-8_27.

[44] M. Pietikäinen, T. Ojala, and Z. Xu, "Rotation-invariant texture classification using feature distributions," *Pattern Recognit.*, vol. 33, no. 1, pp. 43–52, Jan. 2000.

[45] J. Shi, L. Xu, and J. Jia, "Just noticeable defocus blur detection and estimation," in *Proc. IEEE Conf. Comput. Vis. Pattern Recognit. (CVPR)*, Jun. 2015, pp. 657–665.

[46] C. T. Vu, T. D. Phan, and D. M. Chandler, "S_3: A spectral and spatial measure of local perceived sharpness in natural images," *IEEE Trans. Image Process.*, vol. 21, no. 3, pp. 934–945, Mar. 2011.

[47] J. Shi, L. Xu, and J. Jia, "Discriminative blur detection features," in *Proc. IEEE Conf. Comput. Vis. Pattern Recognit.*, Jun. 2014, pp. 2965–2972.

[48] B. Su, S. Lu, and C. L. Tan, "Blurred image region detection and classification," in *Proc. 19th ACM Int. Conf. Multimedia (MM)*, 2011, pp. 1397–1400, doi: 10.1145/2072298.2072024.

[49] S. Zhuo and T. Sim, "Defocus map estimation from a single image," *Pattern Recognit.*, vol. 44, no. 9, pp. 1852–1858, Sep. 2011.

[50] X. Zhu, S. Cohen, S. Schiller, and P. Milanfar, "Estimating spatially varying defocus blur from a single image," *IEEE Trans. Image Process.*, vol. 22, no. 12, pp. 4879–4891, Dec. 2013.

[51] T. Ojala, M. Pietikäinen, and D. Harwood, "A comparative study of texture measures with classification based on featured distributions," *Pattern Recognit.*, vol. 29, no. 1, pp. 51–59, Jan. 1996.

[52] T. Ojala and M. Pietikäinen, "Unsupervised texture segmentation using feature distributions," *Pattern Recognit.*, vol. 32, no. 3, pp. 477–486, Mar. 1999.

[53] T. Ahonen, A. Hadid, and M. Pietikainen, "Face description with local binary patterns: Application to face recognition," *IEEE Trans. Pattern Anal. Mach. Intell.*, vol. 28, no. 12, pp. 2037–2041, Dec. 2006.

[54] M. Pietikäinen, T. Nurmela, T. Mäenpää, and M. Turtinen, "View-based recognition of real-world textures," *Pattern Recognit.*, vol. 37, no. 2, pp. 313–323, Feb. 2004.

[55] M. Heikkila and M. Pietikainen, "A texture-based method for modeling the background and detecting moving objects," *IEEE Trans. Pattern Anal. Mach. Intell.*, vol. 28, no. 4, pp. 657–662, Apr. 2006.

[56] R. Achanta, S. Hemami, F. Estrada, and S. Susstrunk, "Frequency-tuned salient region detection," in *Proc. IEEE Conf. Comput. Vis. Pattern Recognit.*, Jun. 2009, pp. 1597–1604, doi: 10.1109/CVPR.2009.5206596.

[57] F. Perazzi, P. Krahenbuhl, Y. Pritch, and A. Hornung, "Saliency filters: Contrast based filtering for salient region detection," in *Proc. IEEE Conf. Comput. Vis. Pattern Recognit.*, Jun. 2012, pp. 733–740, doi: 10.1109/CVPR.2012.6247743.

[58] J. Ren, X. Jiang, and J. Yuan, "Noise-resistant local binary pattern with an embedded error-correction mechanism," *IEEE Trans. Image Process.*, vol. 22, no. 10, pp. 4049–4060, Oct. 2013.

[59] Z. Wang, Y. Ma, F. Cheng, and L. Yang, "Review of pulse-coupled neural networks," *Image Vis. Comput.*, vol. 28, no. 1, pp. 5–13, Jan. 2010, doi: 10.1016/j.imavis.2009.06.007.

[60] J. Lian, Z. Yang, J. Liu, W. Sun, L. Zheng, X. Du, Z. Yi, B. Shi, and Y. Ma, "An overview of image segmentation based on pulse-coupled neural network," *Arch. Comput. Methods Eng.*, vol. 28, no. 2, pp. 387–403, Mar. 2021, doi: 10.1007/s11831-019-09381-5.

[61] K. Jiao and Z. Pan, "A novel method for image segmentation based on simplified pulse coupled neural network and gbest led gravitational search algorithm," *IEEE Access*, vol. 7, pp. 21310–21330, 2019.

[62] X. Yi and M. Eramian, "LBP-based segmentation of defocus blur," *IEEE Trans. Image Process.*, vol. 25, no. 4, pp. 1626–1638, Apr. 2016.

[63] D. A. Duc, L. H. Van, V. F. Yu, S.-Y. Chou, N. V. Hien, N. T. Chi, D. V. Toan, and L. Q. Dat, "A dynamic generalized fuzzy multi-criteria croup decision making approach for green supplier segmentation," *PLoS ONE*, vol. 16, no. 1, Jan. 2021, Art. no. e0245187, doi: 10.1371/journal.pone.0245187.

[64] M. Singh, "Enhanced image segmentation using fuzzy logic," *Int. J. Electron. Comput. Sci. Eng.*, vol. 2, no. 3, pp. 933–940, 2013.

[65] M. K. Ghorabaee, E. K. Zavadskas, L. Olfat, and Z. Turskis, "Multi-criteria inventory classification using a new method of evaluation based on distance from average solution (EDAS)," *Informatica*, vol. 26, no. 3, pp. 435–451, Jan. 2015.

[66] J.-P. Fan, Y.-J. Li, and M.-Q. Wu, "Technology selection based on EDAS cross-efficiency evaluation method," *IEEE Access*, vol. 7, pp. 58974–58980, 2019.

[67] S. Basar, M. Ali, G. Ochoa-Ruiz, M. Zareei, A. Waheed, and A. Adnan, "Unsupervised color image segmentation: A case of RGB histogram based K-means clustering initialization," *PLoS ONE*, vol. 15, no. 10, Oct. 2020, Art. no. e0240015, doi: 10.1371/journal.pone.0240015.

[68] G. Ilieva, T. Yankova, and S. Klisarova-Belcheva, "Decision analysis with classic and fuzzy EDAS modifications," *Comput. Appl. Math.*, vol. 37, no. 5, pp. 5650–5680, Nov. 2018.

[69] W.-Z. Liang, G.-Y. Zhao, and S.-Z. Luo, "An integrated EDAS-ELECTRE method with picture fuzzy information for cleaner production evaluation in gold mines," *IEEE Access*, vol. 6, pp. 65747–65759, 2018, doi: 10.1109/ACCESS.2018.2878747.

[70] Y.-Y. Li, J.-Q. Wang, and T.-L. Wang, "A linguistic neutrosophic multi-criteria group decision-making approach with EDAS method," *Arabian J. Sci. Eng.*, vol. 44, no. 3, pp. 2737–2749, Mar. 2019.

[71] Ž. Stević, M. Vasiljević, A. Puška, I. Tanackov, R. Junevičius, and S. Vesković, "Evaluation of suppliers under uncertainty: A multiphase approach based on fuzzy AHP and fuzzy EDAS," *Transport*, vol. 34, no. 1, pp. 52–66, Jan. 2019, doi: 10.3846/transport.2019.7275.

[72] G. Mehmood, M. Z. Khan, A. Waheed, M. Zareei, and E. M. Mohamed, "A trust-based energy-efficient and reliable communication scheme (Trust-based ERCS) for remote patient monitoring in wireless body area networks," *IEEE Access*, vol. 8, pp. 131397–131413, 2020, doi: 10.1109/ACCESS.2020.3007405.

[73] F. Shaik, B. V. Reddy, G. V. Pavankumar, and C. Viswanath, "Unsupervised segmentation of image using novel curve evolution method," in *Proc. ICCCE*. Singapore: Springer, 2021, pp. 587–597, doi: 10.1007/978-981-15-7961-5_57.

[74] M. Roy and S. Mukhopadhyay, "A scheme for edge-based multi-focus color image fusion," *Multimedia Tools Appl.*, vol. 79, nos. 33–34, pp. 24089–24117, Sep. 2020, doi: 10.1007/s11042-020-09116-w.

[75] Y. Wen, X. Yang, T. Celik, O. Sushkova, and M. K. Albertini, "Multifocus image fusion using convolutional neural network," *Multimedia Tools Appl.*, vol. 79, nos. 45–46, pp. 34531–34543, Dec. 2020, doi: 10.1007/s11042-020-08945-z.

[76] A. Shen, H. Dong, K. Wang, Y. Kong, J. Wu, and H. Shu, "Automatic extraction of blur regions on a single image based on semantic segmentation," *IEEE Access*, vol. 8, pp. 44867–44878, 2020, doi: 10.1109/ACCESS.2020.2978084.

SADIA BASAR received the M.Sc. degree in computer science from the University of Peshawar, and the M.S. degree in computer science from the Institute of Management Sciences, Peshawar, in 2014. She is currently pursuing the Ph.D. degree with the Information Technology Department, Hazara University Mansehra. She is also working as a Lecturer with the Department of Computer Science, Abbottabad University of Science and Technology (AUST), Abbottabad, Pakistan. Her research interests include multimedia applications, digital image processing, and image segmentation.

MUSHTAQ ALI received the M.Sc. degree in computer science from Gomal University, Pakistan, in 2002, the M.S. degree in computer science from COMSATS University Islamabad, Pakistan, in 2007, and the D.Eng. degree in computer science and technology from the University of Electronic Science and Technology of China (UESTC), in 2015. He is currently a HEC approved Ph.D. Supervisor recognized by the Higher Education Commission (HEC), Pakistan. He is also working as an Assistant Professor with the Department of Information Technology, Hazara University Mansehra. His research interests include digital image processing, content-based image retrieval systems, computer vision, and steganography.

GILBERTO OCHOA-RUIZ received the European Erasmus Mundus master's degree in computer vision and robotics from Heriot-Watt University at Edinburgh, Edinburgh, U.K., and the Ph.D. degree in electronic imaging and computer vision from the Université de Bourgogne, France. He currently works as an Associate Professor—Researcher in artificial intelligence and computer vision with the Machine Learning Group, Tecnológico de Monterrey. His main research interests include computer vision and image processing for applications in medical imaging and video analysis, and the training and deployment of optimized deep learning models in constrained devices for edge computing applications.

ABDUL WAHEED received the master's and Ph.D. degrees in computer science from the Department of Information Technology, Hazara University Mansehra, in 2014 and 2021, respectively. He has completed his Ph.D. research from NetLab-INMC, under the School of Electrical and Computer Engineering (ECE), Seoul National University (SNU), South Korea, in 2019, under the HEC Research Program. He is currently a member of the Crypto-Net Research Group, Hazara University. He also serves as a Lecturer for the Department of Computer Sciences, Iqra National University, Peshawar. He has numerous publications in journals and international conferences. His research interests include information security, secure and smart cryptography, heterogeneous communications within the IoT, mobile *adhoc* networks (MANETs), wireless sensor networks (WSNs) security, and fuzzy logic-based decision-making theory.

GERARDO RODRIGUEZ-HERNANDEZ received the M.Sc. degree in applied artificial intelligence from the University of Exeter, U.K., and the Ph.D. degree in nano materials from the University of Oxford, U.K. He is currently working on the development of AI solutions for the industry, including smart edge computing devices for the IIoT, and the deployment of AI pipelines for a variety of applications. He is currently Coordinator of the Artificial Intelligence Laboratory at CIATEQ, A.C. Mexico. His research interests include artificial intelligence-based applications and smart edge computing devices for the IIoT. He is a member of the Mexican National Researchers System (SNI).

MAHDI ZAREEI (Senior Member, IEEE) received the M.Sc. degree in computer network from the University of Science at Malaysia, Malaysia, in 2011, and the Ph.D. degree from the Communication Systems and Networks Research Group, Malaysia-Japan International Institute of Technology, University of Technology at Malaysia, Malaysia, in 2016. In 2017, he joined the School of Engineering and Sciences, Tecnologico de Monterrey, as a Postdoctoral Fellow, where he has been a Research Professor, since 2019. His main research interests include wireless sensor and *ad hoc* networks, energy harvesting sensors, information security, and machine learning. He is a member of the Mexican National Researchers System (level I). He is serving as an Associate Editor for the IEEE Access and *Ad-Hoc and Sensor Wireless Networks* journals.

• • •